TÜBİTAK

Turkish Journal of Earth Sciences

http://journals.tubitak.gov.tr/earth/

Research Article

Turkish J Earth Sci
(2023) 32: 351-379

doi:10.55730/1300-0985.1849

Internal deformation of continental blocks within converging plates: insights from the Ovacık Fault (Anatolia, Türkiye)

Cengiz ZABCI[1,*], Taylan SANÇAR[2], Dmitry TIKHOMIROV[3,4], Susan IVY-OCHS[5], Christof VOCKENHUBER[5], Anke M. FRIEDRICH[6], Müge YAZICI[1,7], Naki AKÇAR[3]

[1]Department of Geological Engineering, Faculty of Mines, İstanbul Technical University, İstanbul, Turkey
[2]Department of Geography, Munzur University, Tunceli, Turkey
[3]Institute of Geological Sciences, University of Bern, Bern, Switzerland
[4]Department of Geography, University of Zurich, Zurich, Switzerland
[5]Laboratory of Ion Beam Physics, ETH Zürich, Switzerland
[6]Department of Earth and Environmental Sciences, Ludwig Maximilian University of Munich, Munich, Germany
[7]Helmholtz Center Potsdam GFZ German Georesearch Center, Dynamics of the Lithosphere, Potsdam, Germany

Received: 14.03.2022 • **Accepted/Published Online:** 03.12.2022 • **Final Version:** 28.04.2023

Abstract: The active tectonics of Anatolia is mostly characterized by its westward motion with respect to Eurasia between the Hellenic subduction in the west and Arabia-Eurasia continental collision in the east. Although most of the deformation is suggested to be confined along Anatolia's boundary elements, viz. the North and East Anatolian shear zones, recent studies indicate a higher magnitude of internal strain accumulation, especially along the parallel/subparallel strike-slip faults of its central province. We present the first morphochronology-based slip rate estimate for one of these strike-slip structures, the Ovacık Fault, by using cosmogenic ^{36}Cl dating of offset fluvial deposits. At the Köseler Site (39.3643°N, 39.1688°E), two faulted risers, bounding the alluvial fan with its subplanar surface (NF1/NF1') and the inset terrace tread (NF1/T2), are offset 19–24 and 15–22 m, respectively. The scattered surface ages and variability of ^{36}Cl concentrations in depth profiles suggest strong evidence for inheritance in alluvial fan and terrace deposits; thus, we used modelled depth-profile ages for both surfaces. The modelled ages 8–10 ka for NF1 and 6–8 ka for T2 yield slip-rate estimates 2.4 +0.5/–0.4 mm/a and 2.8 +0.7/–0.7 mm/a, respectively, for the upper-tread reconstruction of the NF1/NF1'and the lower-tread reconstruction of the NF1/T2. Our results together with previous slip-rate estimates for other structures show a significant internal deformation for Anatolia, especially along its subparallel strike-slip faults. These secondary faults slice Anatolia into several pieces giving rise to the formation of the Malatya-Erzincan, Cappadocian, and Central Anatolian slices, where the geometry is strongly controlled by the distribution of the Tethyan accretionary complexes.

Key words: Collision, strike-slip faults, slip rate, Anatolia, earthquake

1. Introduction

The rigid pieces of the lithosphere, referred to as 'plates', are believed to move along narrow boundaries due to the theory of plate tectonics (e.g., Wilson, 1965; McKenzie and Parker, 1967; Le Pichon, 1968; Morgan, 1968). Although the 'narrow' nature of plate boundaries is primarily valid in oceanic realms, their continental counterparts are known to have distributed structures and sparse seismicity in general as we observe in Asia, western North America or New Zealand (Molnar, 1988; Stein and Sella, 2002; Şengör et al. 2019a). The width of these 'plate boundary zones' reaches its grandest scale in Central Asia along the Alpide plate boundary zone, where the deformation of the India-Eurasia collision is distributed across the approximately 3000-km-wide region between the Himalayas in the south and the Baikal Rift in the north being mainly confined to the accretionary complexes of the Tethysides and the Altaids (Molnar and Tapponnier, 1975; Tapponnier et al., 1986; Şengör et al., 1993; Şengör and Natal'in, 1996; Şengör et al., 2018). Continental deformation may exhibit quite inhomogeneous styles and distribution of tectonic elements, such as (a) overthrusting of slivers of India's northern margin onto the rest of the subcontinent (Himalayas), (b) numerous faults slicing the Tibetan Plateau, (c) the undeformed Tarim Basin, or (d) the discrete structures of t h e Kzahkstan-Dungaria-Mongolia provinces in Asia (Molnar, 1988; Avouac and Tapponnier, 1993; Şengör and Natal'in, 1996). Some of these structures generate major block-boundary elements, like the Altyn Tagh and Kunlun faults in the

* Correspondence: zabci@itu.edu.tr

Tibetan Plateau (Tapponnier and Molnar, 1975; Avouac and Tapponnier 1993) or the San Andreas Fault in the western North America (Wallace, 1990) with intense and relatively frequent seismicity due to their moderate (5 to 10 mm/a) to high (>10 mm/a) magnitude of annual slip-rate (e.g., Sieh and Jahns, 1984; Mériaux et al. 2004, 2005, 2012; Meade and Hager, 2005; van der Woerd et al., 1998, 2000, 2002; Gold et al. 2009). Discrete members of these plate boundary zones may also have very large but less frequent earthquakes with magnitudes reaching M=8 or even higher along faults with slow slip rates (<5 mm/a), e.g., M= 8.7 1920 Haiyuan (Weiqi et al., 1987), M=8.4 1905 Bulnay (Okal, 1977; Schlupp and Cisternas, 2007) and M=8.1 1957 Bogd earthquakes (Baljinyam et al., 1993; Kurushin et al., 1997). Therefore, it is essential to quantify the active deformation of all structures in such regions not only for local earthquake hazard assessments, but also for a better understanding on the distribution and style of deformation in the continental crust/lithosphere.

Anatolia (and adjacent regions) is one of the ideal places to study the active continental deformation due to its unique location in the Alpide plate boundary zone (Şengör et al., 1985; Şengör and Natal'in, 1996). Hereby, the deformation is mostly characterized by the relative westward motion of Anatolia with respect to Eurasia between the Hellenic Subduction in the west and the Arabia-Eurasia continental collision in the east (McKenzie, 1972; Şengör et al. 1985), where the width of the Alpide plate boundary zone decreases relatively to a narrow zone (especially with respect to Central Asia), hardly exceeding 600 km (Şengör and Natal'in, 1996; Stein and Sella, 2002; Şengör et al., 2019a). Although the early GNSS-based studies suggest that almost all of this present-day motion happens mainly along the 'block' boundary structures, the North Anatolian (NASZ) and East Anatolian (EASZ) shear zones (e.g., Reilinger et al., 2006), recent studies of various disciplines provide a more complex tectonic picture for the internal parts of Anatolia and a higher magnitude of strain, especially along its subparallel strike-slip faults (e.g., Kaymakçı et al., 2006; Özener et al., 2010; Aktuğ et al., 2013a; Aktuğ et al., 2013b; Higgins et al., 2015; Sarıkaya et al., 2015; Yıldırım et al., 2016; Sançar et al., 2020; Özbey et al., 2022). The Malatya-Ovacık Fault Zone (MOFZ) is one of these strike-slip structures, which was suggested to have marked the eastern boundary of Anatolia of about 5 Ma ago but to bein active today based on early kinematicmodels (Westaway and Arger, 2001; Westaway et al., 2008). However, recent geodetic (Aktuğ et al., 2013a; Aktuğ et al., 2013b; Özener et al., 2020), structural (Kaymakçı et al., 2006), palaeoseismological (Sançar et al., 2019; Yazıcı et al., 2021), geomorphological (Yazıcı et al., 2018; Sançar et al., 2020) and seismological (Acarel et al., 2019) studies show the opposite yielding significant tectonic activity along the MOFZ.

We conducted a new geologic slip-rate study by using cosmogenic 36Cl ages of offset alluvial fan and terrace deposits at the Köseler Site along the northeastern member of the MOFZ, the Ovacık Fault (OF). In addition to our results, we compiled available palaeoseismological studies along the other 'internal' structures of Anatolia, and attempted a synthesis to better understand the nature of rigid or semi-rigid behaviour of this body. This study's results contribute to the earthquake hazard assessment of the OF and the surrounding region and provide information on the origin and mechanism of the internal deformation of Anatolia and similar tectonic regions elsewhere on the earth.

In this paper, we write figure with a lowercase "f" for figures we cite from the literature and Figure with a capital "F" for our own figures in this paper.

2. Tectonic setting and the geology of the study region

2.1. Active tectonics of Anatolia and the Malatya-Ovacık Fault Zone

The interaction of three major plates Eurasia, Africa, Arabia, and the smaller Anatolian *Scholle* creates a complex tectonic setting, which is mainly controlled by the Zagros subduction-collision and/or the Hellenic subduction and rollback, in the eastern Mediterranean (McKenzie, 1970; 1972; Şengör et al., 1985; Reilinger et al., 2006; Le Pichon and Kreemer, 2010; Şengör and Yazıcı, 2020). In this complex tectonic region, the westward motion of Anatolia relative to Eurasia is driven by (a) tectonic escape system caused by the postcollisional convergence of Eurasia and Arabia creating forces at its boundaries (McKenzie, 1970; 1972; Şengör et al., 1985), (b) the additional support from the buoyancy force from the gravitational potential of the East Anatolia High Plateau (McKenzie, 1972; Şengör et al., 1985; Özeren and Holt, 2010), (b) slab pull of the Hellenic subduction (Chorowicz et al., 1999; Reilinger et al., 2006), (c) asthenospheric flow dragging the circular motion of lithosphere from the Levant in the east to Anatolia and Aegean in the west (Le Pichon and Kreemer, 2010), (d) combination of the effect of slab pull with a mantle upwelling underneath Afar and with a large-scale flow associated with the whole mantle (Faccenna et al., 2013), (e) the balance between internal gradients of Gravitational Potential Energy within the continental lithosphere of the region (England et al., 2016) or (f) combinations of these mechanisms (e.g., Paul et al., 2014; Şengör and Yazıcı, 2020). These driving mechanisms and related structures define four major neotectonic provinces in Türkiye, which are: (1) the East Anatolian province of shortening (EAPS), (2) the West Anatolian extensional province (WAEP), (3) the North Turkish province (NTP), and (4) the Central "ova" province (COP) (Figure 1). Two major strike-slip fault systems, the NASZ and the EASZ, form the

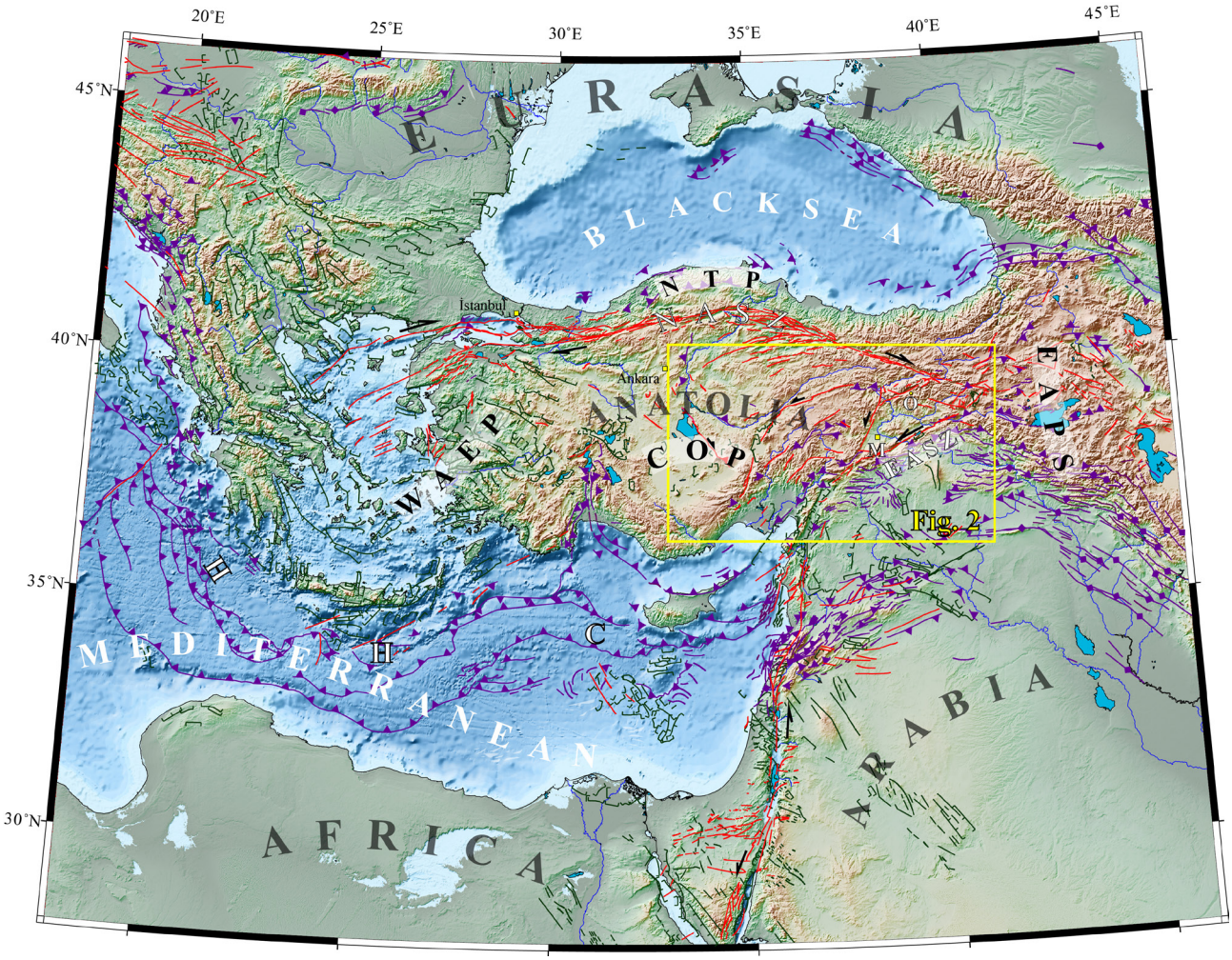

Figure 1. Neotectonic structures of the eastern Mediterranean, which are late medial Miocene (13 Ma) or younger (Şengör and Zabcı, 2019; Şengör et al., 2019a). All red lines show strike-slip faults, whereas the green is for extensional and the purple colour is for compressional structures. The yellow rectangle marks the geographical extent of the region of interest (Figure 2). Key to lettering: H, Hellenic Trench; C, Cyprus Trench; M, Malatya; O, Ovacık; NASZ, North Anatolian Shear Zone; EASZ, East Anatolian Shear Zone; WAEP, West Anatolia Extensional Province; EAPS, East Anatolia Province of Shortening; COP, Central Anatolia 'ova' Province; NTP, North Turkish Province.

boundaries between some of these provinces (Şengör et al., 1985; Şengör and Yazıcı, 2020).

The Central "ova" province, the second quietest following the north Turkish province in terms of seismic activity. Most of its neotectonic features lie buried under extensive pluvial lake sediments (Şengör, 1980; Şengör et al., 1985). Şengör (1979) compares the faults of the "ova" province with the slip lines of the modified Prandtl cell model and suggests a causal relationship between the NASZ and the EASZ, and the tectonic structures of the internal parts of Anatolia. Later studies document mostly NW-striking dextral and NE-striking sinistral strike-slip faults (see Bozkurt (2001) for a review of these neotectonic structures) in the central Anatolia, supporting passive Prandtl cell model of Varnes (1962) (Sançar et al., 2018). Higgins et al. (2015) propose that these second-order strike-slip faults are likely shallow upper crustal structures, which divide central and eastern Anatolia into smaller blocks under the influence of the Aegean extension. According to Şengör et al. (2019a), these slices are believed to move synthetic to the North Anatolian Keirogen (the main continental transform system that includes the NASZ and the North Anatolian Fault), forming a keirogen-parallel shortening due to rotation (Şengör et al., 2019a). This shortening is distributed within the rotating slices and generates E-W-trending folds and thrusts in addition to NE-striking sinistral and NW-striking dextral strike-slip faults (see figures 28a and 28b in Şengör et al.

(2019a)). Alternatively, the NE-striking sinistral strike-slip faults within Anatolia are linked and interpreted with the migrating wedge model, in which the escape wedge has propagated from west to east by successive jump stages and the EASZ represents the eastern boundary today as its last stage (Chorowicz et al., 1999).

The Malatya-Ovacık Fault Zone (MOFZ) is one of the NE-striking sinistral faults of the central "ova" province that splays from the NASZ near Erzincan (Figure 1). It runs in approximately N65–70° strike for about 110 km (Ovacık Fault – OF) and then bends into SSW direction (Malatya Fault, MF) and terminates close to Doğanşehir, Malatya (Figure 2). This fault zone is interpreted to be the former eastern boundary of Anatolia, which was only active between 5 and 3 Ma and took up a total of 29 km of relative motion between Arabia and Anatolia (Westaway and Arger, 2001). Another kinematic model also argues for a similar origin for this tectonic feature, which was claimed to be active between approximately 7–6 and 3.5 Ma and having an of 8 km offset (Westaway et al., 2008). However, multiple views suggest that the MOFZ, there are multiple views suggesting that this tectonic structure is still active and takes-up part of the present-day relative motion between Arabia and Anatolia (Koçyiğit and Bayhan, 1998) with a total sinistral displacement of 12.5–20 km for the last 13 Ma (Chorowicz et al., 1995). The tectonic scarps on the modern alluvial fans deposits at the northern margin of the Ovacık Basin (Arpat and Şaroğlu, 1975), morphological response to active deformation (Yazıcı et al., 2018), palaeoseismology

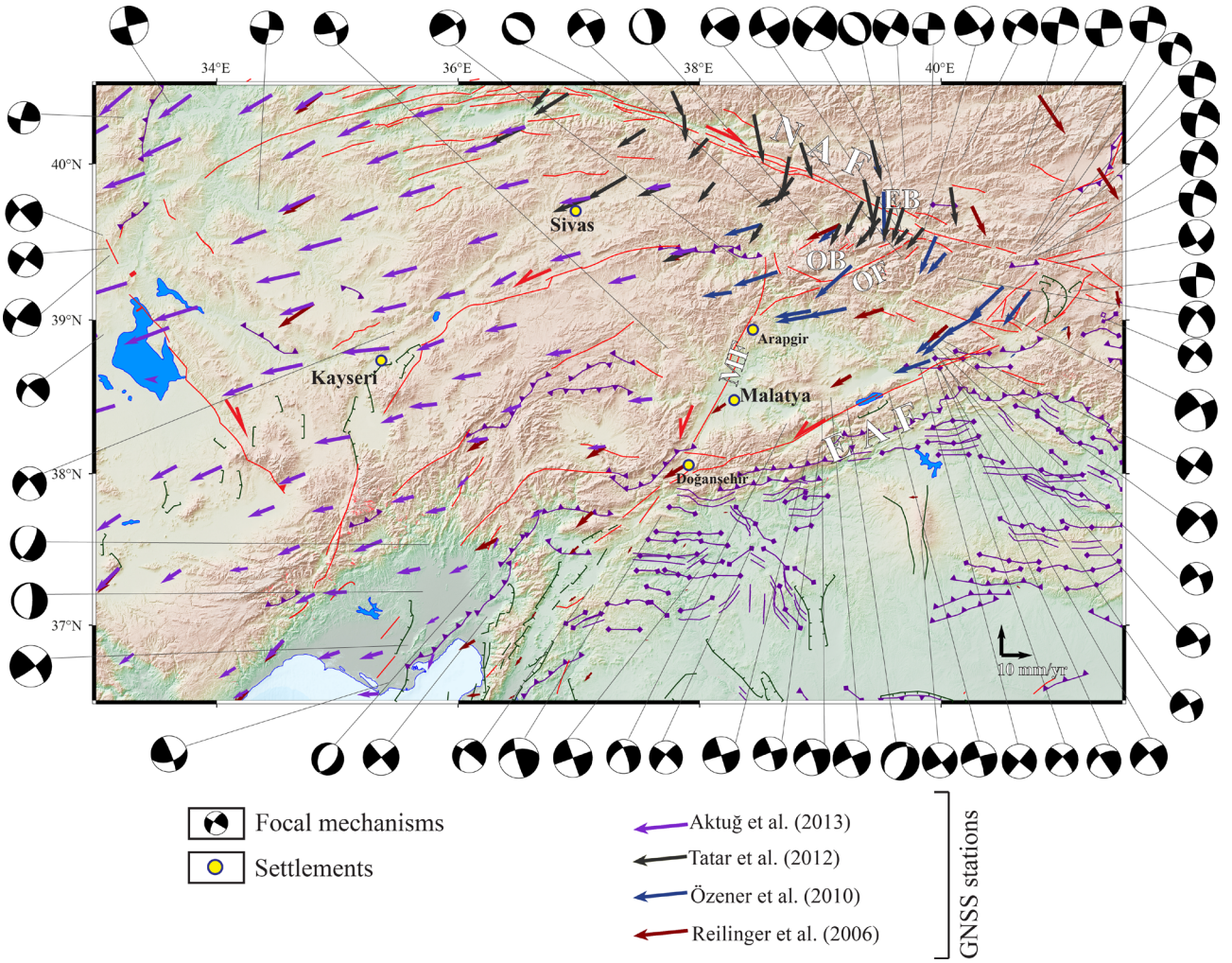

Figure 2. Map showing the study region. The neotectonic structures are from Şengör and Zabcı (2019). The arrows are for GNSS measurements (Aktuğ et al., 2013b; Özener et al., 2010; Reilinger et al., 2006; Tatar et al., 2012), which all are replotted according to the fixed Arabia. Focal mechanisms are from CMT Harvard Database (Ekström et al., 2012). The basemap is the hill shade relief derived from SRTM 1-Arc second dataset (USGS). Key to lettering: GNSS, Global Navigation Satellite System; EAF, East

(Sançar et al., 2019; Yazıcı et al., 2021) and structural data (Kaymakçı et al., 2006) clearly support an ongoing tectonic activity along the OF and MF. Moreover, microseismic activity close to the junction of the OF and MF (Acarel et al., 2019), and local global navigation satellite system (GNSS) measurements covering the region (Aktuğ et al., 2013a; Aktuğ et al., 2013b; Özener et al., 2010) indicate a larger strain accumulation along these structures than previously estimated. The GNSS-based elastic block model slip rates are 1.2 ± 0.3 mm/a and 1.6 ± 0.3 mm/a (Aktuğ et al., 2013a) or 1.8 ± 0.1 and 1.2 ± 0.1 mm/a (Aktuğ et al., 2013b) for two distinct members of this fault zone, the OF and MF, respectively. On the other hand, very long-term geological rate estimates suggest a slightly slower rate of approximately 1 mm/a for the MF (Sançar et al., 2020), while approximately 2.7 mm/a horizontal rate of the western OF (Yazıcı et al., 2021) highly exceeds these short-term values. This difference in geological deformation rates is also supported by paleoseismic records, which yield mean interevent times of 2275 ± 605 years for the MF (Sançar et al., 2019) and 2400 ± 765 years for the OF (Yazıcı et al., 2021). Even though the OF's calculated mean interevent time is similar to the value for the single strand MF, the records from the OF are recovered from a single segment of a wider deformation zone made of multiple parallel/subparallel structures (Yazıcı et al., 2021), thus requires a higher deformation rate in total.

2.2. Geology of the Ovacık Basin and the surrounding region

The Ovacık Basin and its surrounding are characterized by various lithological units. Almost all rocks to the north of the basin are made of Triassic–Cretaceous limestones, whereas different types of lithologies are exposed at other sides, including mostly metamorphics (schists, recrystallized limestones, marbles, metaperidotites, etc.), volcanics, and siliciclastics (Tarhan, 2008). These pre-Quaternary units are covered by fluvial and glacial deposits within the basin's interior (Figure 3). At the margins of the Ovacık Basin, glacial deposits are mostly linked with the widespread glaciation in the Munzur Mountains (Bayrakdar et al., 2015; Yeşilyurt et al., 2015; Akçar et al., 2017; Çılğın et al., 2020). We observe broad alluvial fans at the northern and southern margins of the Ovacık Basin, whereas the central part is dominated by the fluvial sediments of the Munzur River. Although terraces of the Munzur River are mostly limited to a very narrow space of only about 100-m-wide in the east, the width of these fluvial deposits exceeds 1 km to the west of the basin. Glacial deposits are partly preserved at flanks of the secondary modern river channels to the north, where these

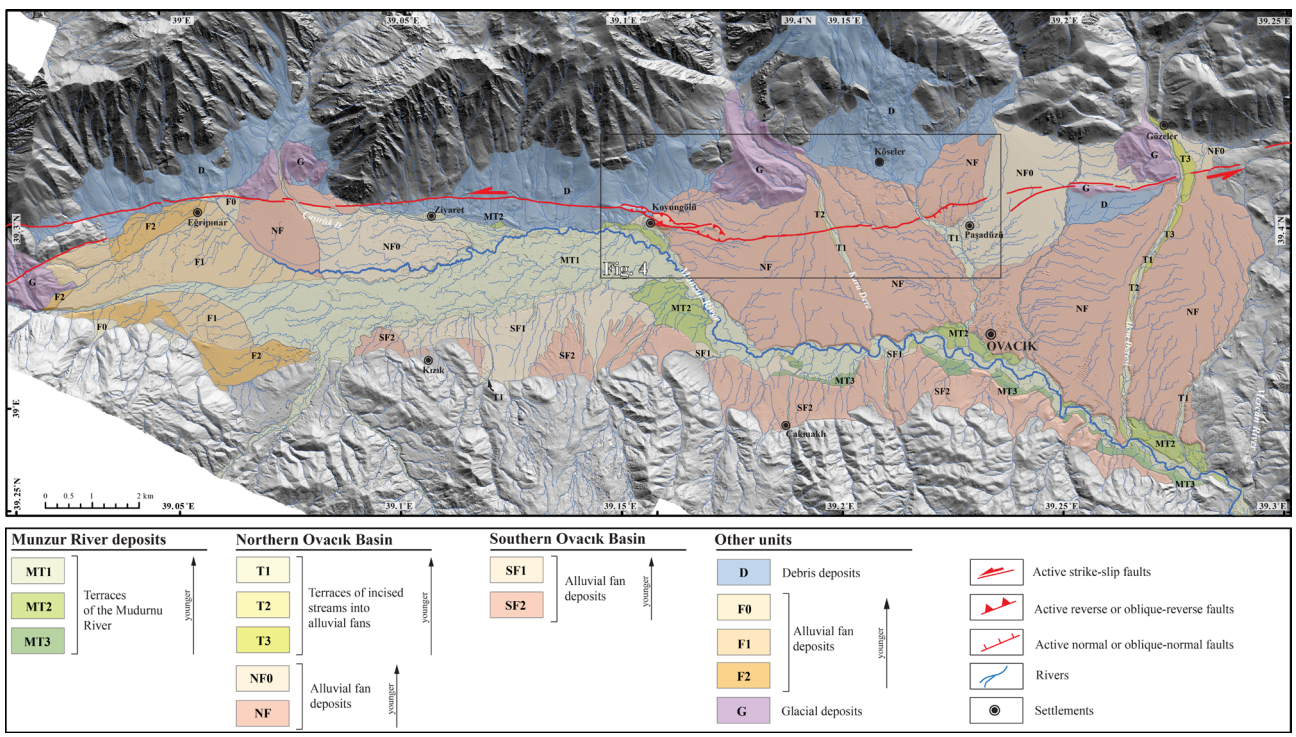

Figure 3. Map showing the Quaternary deposits and active structures at the Ovacık Basin (OB). The basin is mostly defined by alluvial fan and debris deposits at its northern and southern margins, whereas the central part is dominated by the fluvial sediments of the Munzur River. The Ovacık Fault (OF) is clearly marked along a linear scarp, cutting the alluvial fan system and the debris deposits at the northern margin of the OB. The black rectangle marks the geographical extent of Figure 4.

large former glacial valleys of the Munzur Mountains meet with the flat topography of the Ovacık Basin. Especially two of these northern streams, Kuru Dere and Aksu Deresi, are characterized by incised channels into the widely distributed alluvial fans (shown by NF1 in Figures 3–7).

3. Materials and methods

3.1. Mapping and offset determination

Our field and mapping studies for the Köseler Site include surficial geological mapping, offset determinations and sampling for geochronology. The key geomorphic features were mapped in the field using digital aerial photos

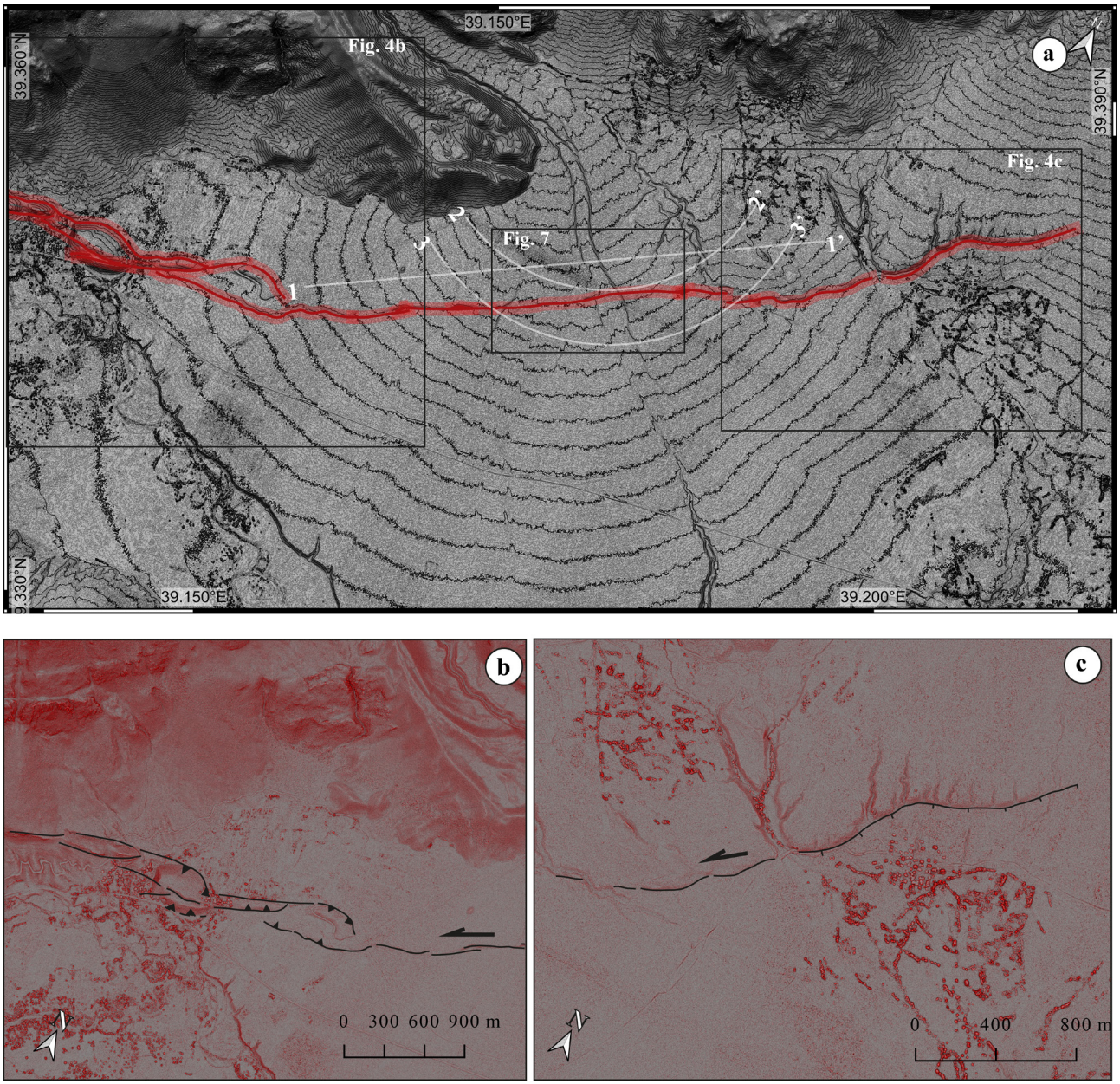

Figure 4. (a) Morphology of the alluvial fan and the geometry of the OF. The map includes elevation contours per 0.25 m (heavy lines each 5 m), which are draped over the DSM of the area. Western and eastern black rectangles show the coverage of the Red Relief Image Maps (RRIM) for regions with complex deformation. The middle one marks the location of the Köseler Site. The white line and arcs are for topographic profiles. **(b)** The restraining step-over geometry of the Ovacık Fault (OF) close to the Koyungölü Village. The uplifted and elongated ridges are the most dominant morphological features, which are delimited by the structural elements of this step-over. **(c)** The releasing bend and its extensional morphology to the north of the Paşadüzü Village. Here, the southern side of the OF is downthrown due to the local vertical component of deformation.

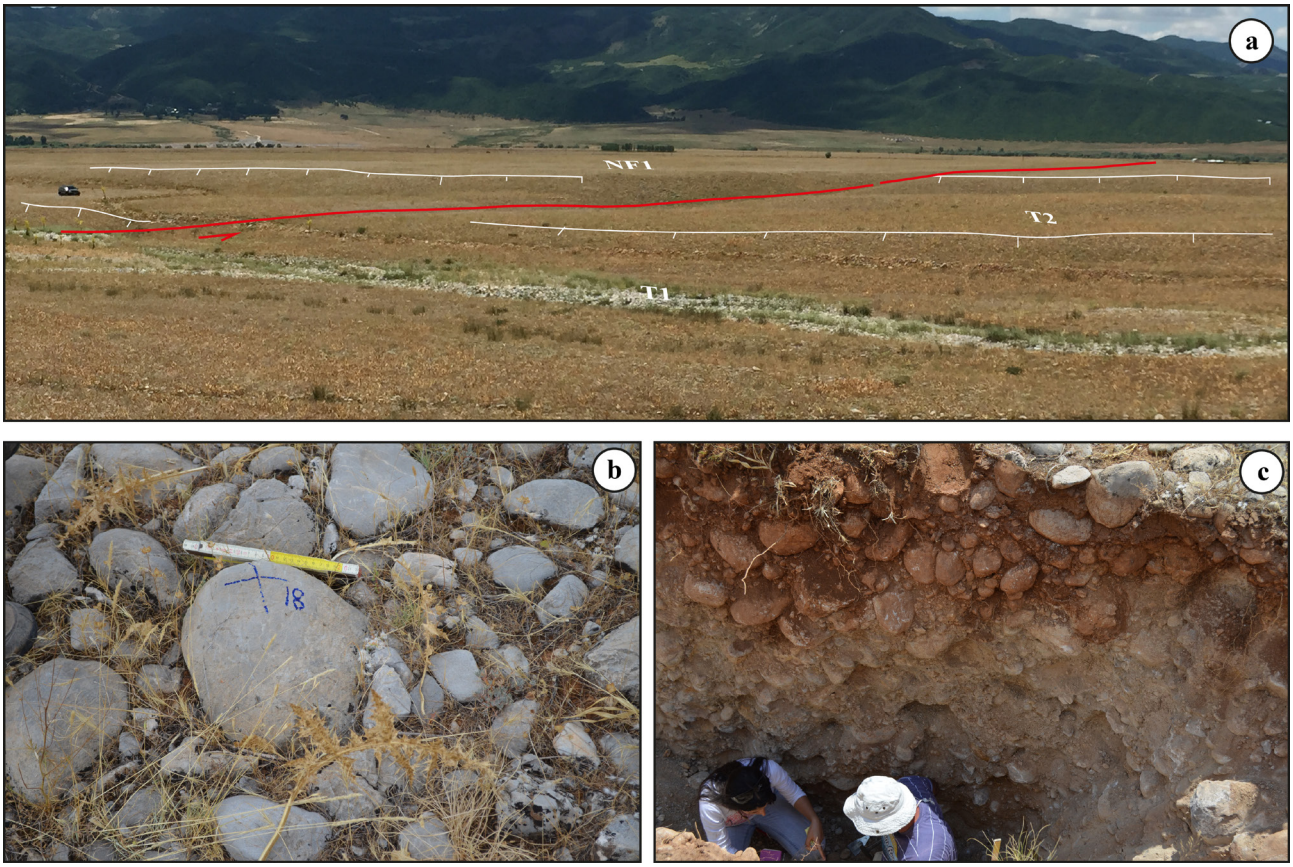

Figure 5. (a) Photograph showing the alluvial fan surface and the inset terraces of the Köseler site. The red solid line is the trace of the Ovacık Fault. Solid white lines indicate the terrace risers with hachures showing the riser escarpment. The view is to the south-southwest. **(b)** Partly buried cobbles and boulders which are densely distributed along both alluvial fan and terrace surfaces. The largest ones were selected for surface sampling. **(c)** Trench in the T2 terrace. The exposure is made of boulders and cobbles within a sandy matrix all down to its bottom.

(orthorectified to approximately 0.4 cm ground pixel resolution) and the stereoscopic aerial photo-based Digital Surface Model (DSM). In the construction of the DSM, we used the semiautomated workflow of Agisoft Metashape Pro to align 92 digital aerial photos and to extract a dense point cloud for the Ovacık Basin. The final DSM was produced based on this depth model with 0.9 m ground-pixel resolution.

By using this spatial dataset and field observations, we document sinistral offsets across risers between the alluvial fan surface (NF1), the strath terrace (T2) and the subplanar inactive fan surface (NF1') at the Köseler Site (Figures 3–9). We used the MATLAB-based software LaDiCaoz_v2v2 to measure lateral displacements (Haddon et al., 2016; Zielke and Arrowsmith, 2012). First, we loaded our high-resolution DSM into the program and trace the fault. Then, fault parallel profiles were placed on each block (red and blue lines in Figures 8a and 9b). Offset geomorphic markers, NF1/T2 and NF1/NF1' risers in our cases, were projected into the fault zone, which were used to reconstruct the preslip topography for each separate case to calculate the optimum slip value. In addition, the min and max slip limits were controlled by incrementally restoring the displacement for each geomorphic marker, using the same program (Figures 8b and 9b). We also took into account 1 m trapezoid error margin for slip measurements in order to include any possible riser degradation. All offset measurements are represented to define only their upper and lower limits (e.g., 17–22 m), and they do not include error margins related to riser degradation within our text or figures.

3.2. Age control

The use of cosmogenic nuclides as a dating tool in Quaternary sciences is unique and widely recognized (Dunai, 2010). Formation of either aggradational (e.g., moraines, mass-movement deposits, alluvial fans and fluvial terraces) or degradational (e.g., strath terraces) or erosional (e.g., ice-moulded bedrock, fault scarps, and wave-cut platforms) landforms can directly be time-calibrated (cf., Ivy-Ochs et al., 2013). The accumulation

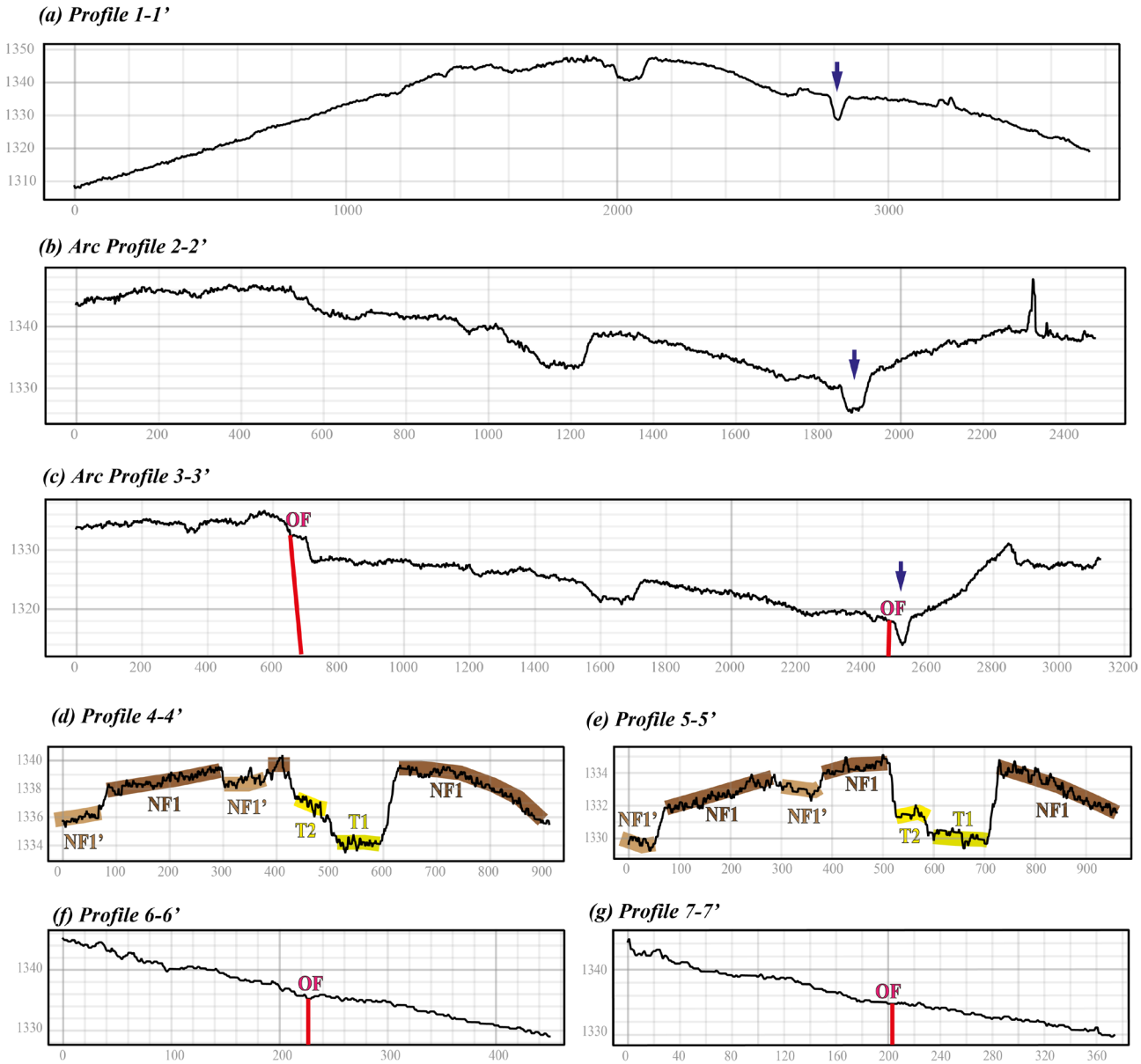

Figure 6. Straight or arc topographic profiles along various paths. For exact locations please see Figures 4 and 7. Straight profiles are mostly oriented parallel (1-1' 4-4' and 5-5') or perpendicular (6-6') to the OF, whereas the arc ones are chosen according to general distribution path of the alluvial fan (apex as being the centre of a circle). **(a)** The fault parallel profile 1-1' represents an identical plano-convex fan morphology (e.g., Blair and McPherson, 1994)). **(b and c)** Arc profiles showing higher surfaces at the easternmost and westernmost flanks of the fan. Please note that a distinct channel follows (marked with blue arrow in a, b, and c) the topographic flexure acting as a boundary with the eastern high and the NF1 surface. **(d and e)** Parallel straight profiles, to the north and south of the OF, showing the NF1 surface, the inactive subplanar fan surface NF1', and terraces (T1 and T2) of the inner active channel. Fault perpendicular profiles **(f and g)** display almost no clear vertical offset.

of cosmogenic nuclides is most often used to date the exposure of surfaces (surface exposure dating) or geologic layers (depth-profile dating). Surface exposure dating utilizes the fact that the production rate is known; thus, when the concentration is measured, the duration since the exposure can be determined (Dunai, 2010). On the other hand, depth-profile dating uses the predictable decrease in cosmogenic nuclide accumulation, which goes along known physical principles (Hancock et al., 1999). Surface exposure and depth-profile dating tools can effectively be applied through a time range from the Pliocene to the late Holocene based on the postformational preservation and exposure histories (Ivy-Ochs and Kober, 2008).

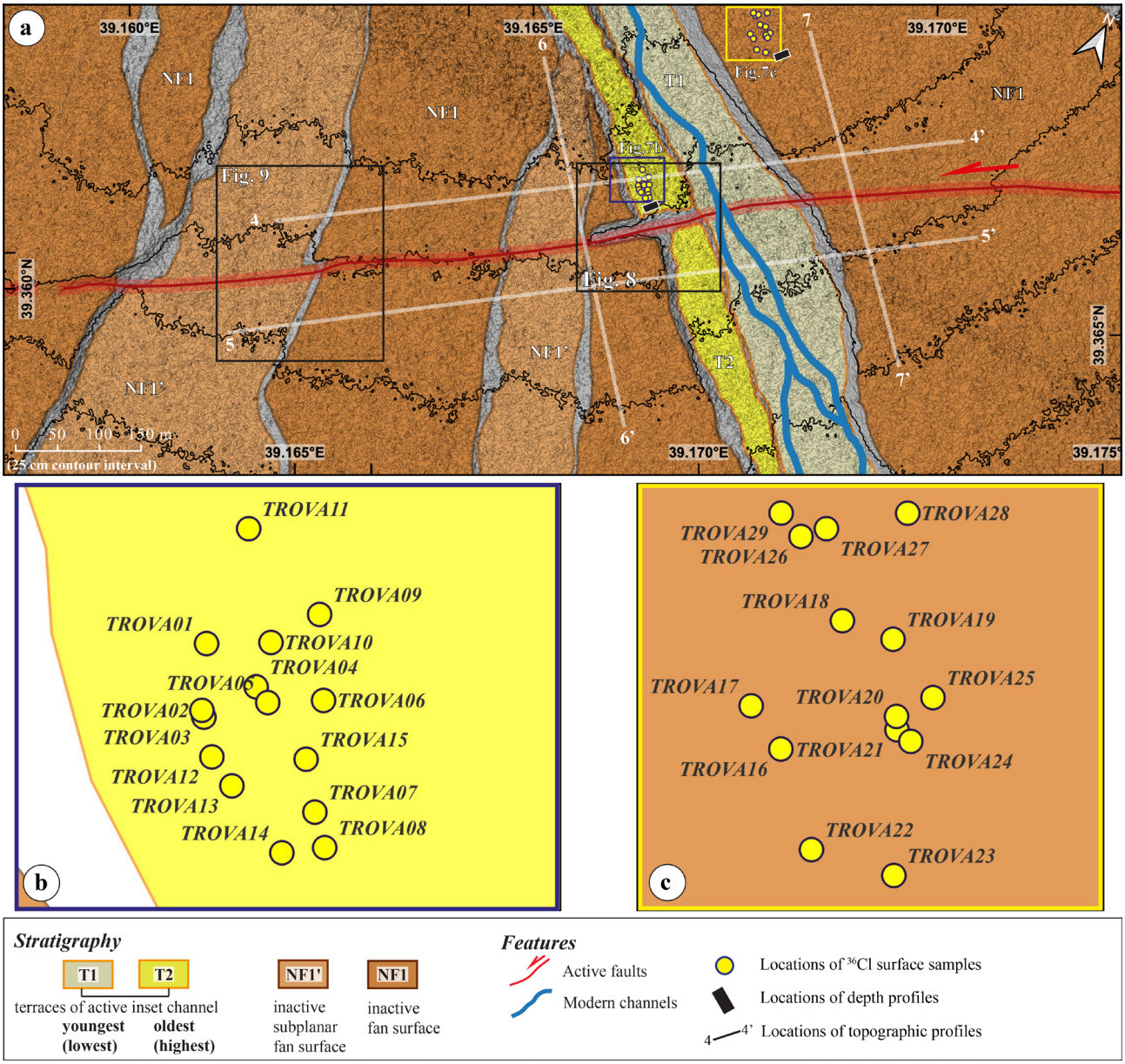

Figure 7. Topographic and surface geological map of the Köseler Site. The active south flowing stream channel is incised into a broad alluvial fan (NF1) and forms a single-paired strath terrace (T2) at its western flank. The NF1 also exhibits lower surfaces—inactive subplanar fan surfaces (NF1'), which were generated by former distributary channels. There are two distinct apparent offsets, NF1/T2 and NF1/NF1' across boundaries of these morphological elements that are marked with black rectangles.

In order to reconstruct the timing of the alluvial fan deposition and the formation of the strath terrace in our study region, we collected surface samples from twentynine coarse limestone cobbles embedded in the alluvial fan and terrace deposits for cosmogenic 36Cl analysis (Figure 7 and Table 1). In addition, we opened two trenches in the alluvial fan and the strath terrace downward for about 2 m and collected eleven sand-sized sediment samples from the matrix between the courser clasts (pebbles and cobbles). In surface sampling, the uppermost 3 to 5 cm parts of the cobbles were sampled with a hammer and chisel following the strategies presented in previous studies (e.g., Akçar et al., 2011). Surfaces of the studied geomorphic units did not show any evidence of disturbance, i.e. there was no mixing and limited soil formation in the upper parts of the sediments close to the surface. We also observed this in the sediment profiles in the trenches (Figures 5b and 5c). To avoid any postdepositional displacements of cobbles, we selected only coarse-cobbles that are embedded in the sediment. Sampled top cobble surfaces were from around

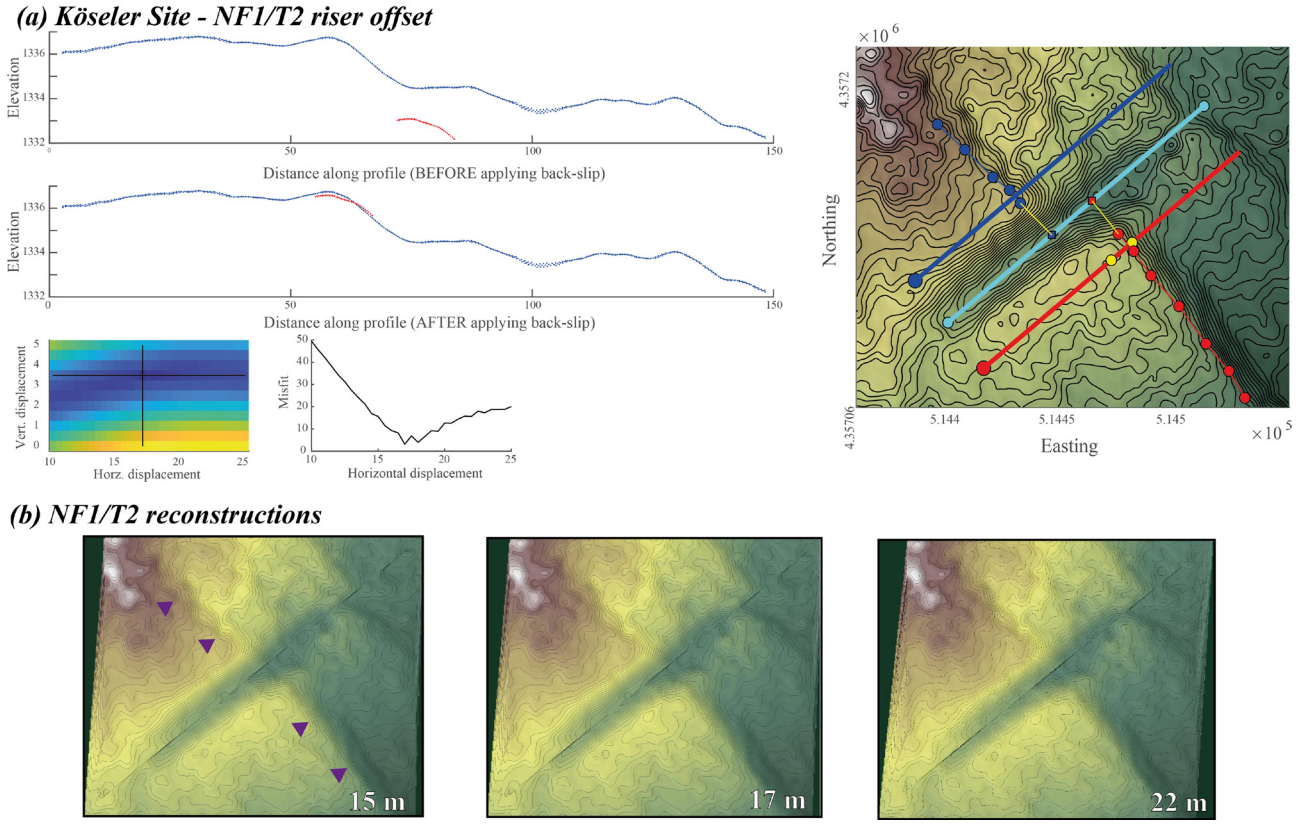

Figure 8. LaDiCaoz analysis of NF1/T2 offset. **(a)** shows the before/after back-slip of fault-parallel profiles projected on the fault plane, whereas the map on the right presents the location of profiles and orientation of the reference feature, NF1/T2 riser in this case. **(b)** Incremental offset reconstructions for 15, 17, and 22 m, which all make the min and max boundaries of our boxcar slip model in our calculations.

10 cm above the surrounding ground (please see Table 1 for further sample information).

For accelerator mass spectrometry (AMS) analysis of cosmogenic ^{36}Cl, samples were processed at the Surface Exposure Laboratory of the University of Bern. For cosmogenic ^{36}Cl, the sample preparation protocol was applied using isotope dilution (Elmore et al., 1997; Ivy-Ochs et al., 2004; Desilets et al., 2006) as described in Akçar et al. (2012), which is based on the method of Stone et al. (1996). We sent a leached aliquot of approximately 10 g from each sample to SGS Laboratories, Toronto, Canada, for elemental analysis (major elements: most importantly Ca, K, Sm, U, Th, B, and Gd) in order to determine the local ^{36}Cl production rate. Table 2 shows major and trace element concentrations of the samples. Both total Cl and ^{36}Cl were measured from one target with isotope dilution at the ETH AMS facility (Synal et al., 1997). The ETH internal standard K382/4N with a value of 17.36×10^{-12} for ^{36}Cl/Cl (normalized to the Nishiizumi standard in 2009) were used to normalize the measured ^{36}Cl/^{35}Cl ratios. The natural ratio ^{37}Cl/^{35}Cl = 31.98% of K382/4N standard and the machine blank was applied to normalize the stable ^{37}Cl/^{35}Cl.

To calculate ^{36}Cl exposure ages, local production rates of cosmogenic ^{36}Cl were scaled according to the Lal (1991) / Stone (2000) (St) scheme and calculated by using a spallogenic production rate of 48.8 ± 1.7 atoms g^{-1} Ca a^{-1} at SLHL as the from Ca (Stone et al., 1996; Stone et al., 1998) and 162 ± 24 atoms g^{-1} K a^{-1} from K (Evans et al., 1997). We applied a production rate of 5.3 ± 0.5 atoms g^{-1} Ca a^{-1} at SLHL due to muon capture (Stone et al., 1996; Stone et al., 1998). To determine ^{36}Cl produced by capture of thermal and epithermal neutrons, we used a rate of 760 ± 150 neutrons g^{-1} a^{-1} above the surface following Liu et al. (1994) and Phillips et al. (2001) (see Alfimov and Ivy-Ochs, 2009 for further details). Major element, boron, gadolinium and samarium concentrations was used to calculate the contribution of low-energy neutrons present for capture by ^{35}Cl to produce ^{36}Cl (Fabryka-Martin, 1988; Phillips et al., 2001; Alfimov and Ivy-Ochs, 2009). We considered uranium and thorium concentrations to determine the fraction of noncosmogenic subsurface ^{36}Cl (Fabryka-Martin, 1988). In the calculation of ^{36}Cl exposure ages, we accounted for: (1) the topographic shielding, calculated after Tikhomirov et al. (2014) based

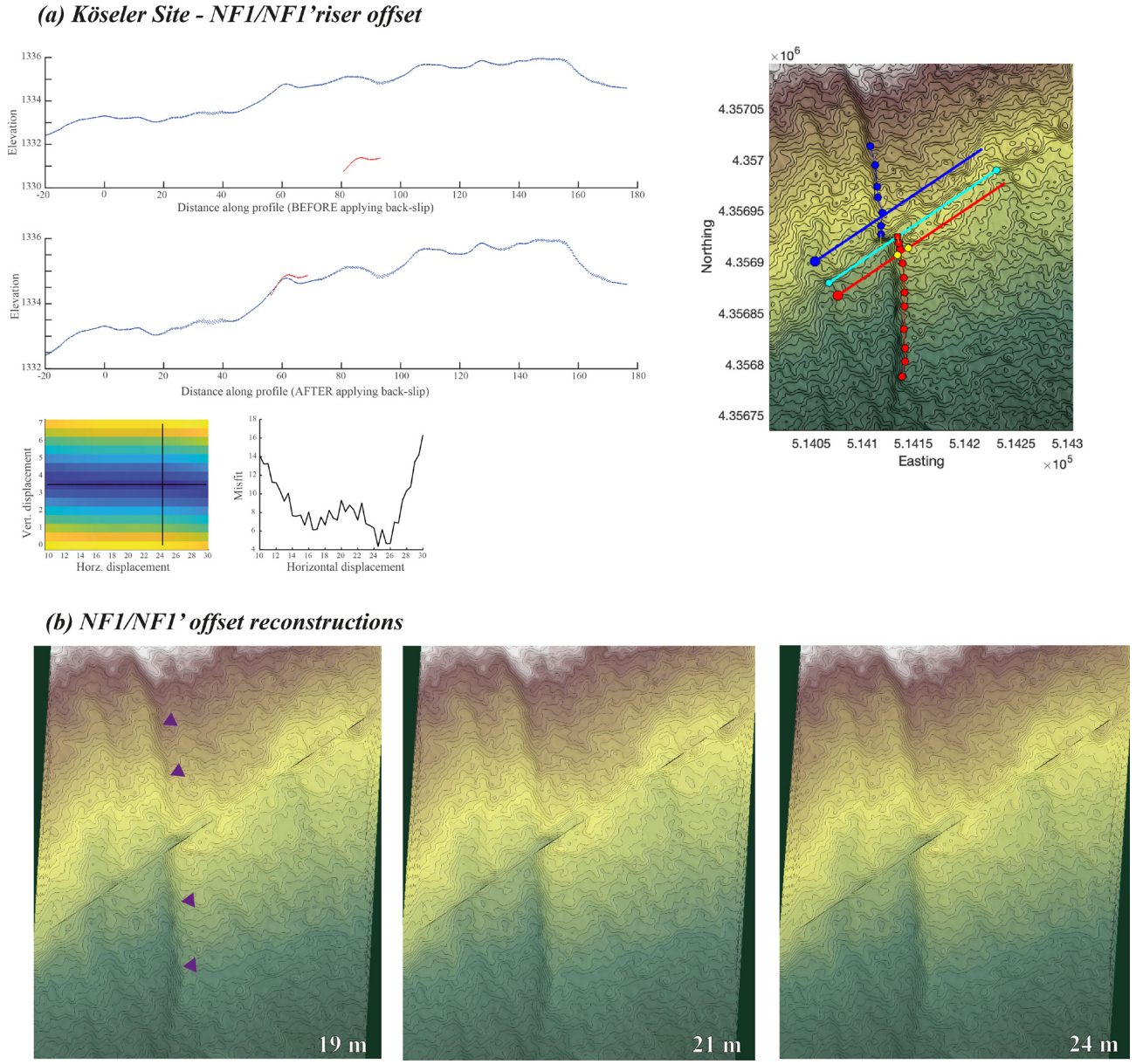

Figure 9. LaDiCaoz analysis of NF1/NF1' offset. **(a)** shows the before/after back-slip of fault-parallel profiles projected on the fault plane, whereas the map on the right presents the location of profiles and orientation of the reference feature, NF1/NF1' riser in this case. **(b)** Incremental offset reconstructions for 19, 21, and 24 m, which all make the min and max boundaries of our boxcar slip model in our calculations.

on Dunne et al. (1999); (2) the sample thickness, using an exponential attenuation length of 160 g/cm^2; and (3) the rock density of 2.40 g/cm^3 for limestone. The contribution of the topographic shielding to exposure ages is less than 1% with a correction factor of 0.99625. To pace the track of weathering, we excavated all the sampled cobbles and we did not observe any difference (trace of weathering) on the sampled surfaces of cobbles in comparison to their buried surfaces. Therefore, we did not apply any erosion correction. Calculated ^{36}Cl exposure ages are given in Table 1 and their probability distributions are shown in Figure 10.

For the depth profiles opened in the alluvial fan (NF-1) and strath terrace (T2), we modelled variations of cosmogenic ^{36}Cl production and calculated cosmogenic ^{36}Cl theoretical concentrations for exposure times between 5 ka and 15 ka. For these, we used the chemical composition and depth of each sample and the method of calculation provided by Alfimov and Ivy-Ochs (2009). As in the exposure age calculations, we applied the same production

Table 1. Cosmogenic ^{36}Cl data and exposure ages of the samples from the Köseler site.

Morphologic unit	Sample name	Altitude (m a.s.l)	Latitude °N (DD.DD)	Longitude °E (DD.DD)	Sample thickness (cm)	Sample depth (cm)	Rock dissolved (g)	^{35}Cl spike (mg)	Cl (ppm)	^{36}Cl (10^4 at g^{-1})	Exposure age (ka)
Strath terrace (T2)	TROVA-1	1334	39.36415	39.1674	4		85.7941	2.424	24.4 ± 1	125.4 ± 7.34	21.5 ± 1
	TROVA-2	1332	39.36409	39.16744	5		86.527	2.438	25.5 ± 1	71.81 ± 3.84	12.2 ± 1
	TROVA-3	1332	39.36408	39.16744	4		87.7431	2.43	22.6 ± 1	87.7 ± 4.62	15 ± 1
	TROVA-4	1332	39.36413	39.16748	4		87.521	2.432	40.7 ± 2	200.67 ± 11.1	33.3 ± 2
	TROVA-5	1329	39.36412	39.1675	5		85.5083	2.438	21.2 ± 1	84.37 ± 3.62	14.6 ± 1
	TROVA-6	1331	39.36415	39.16756	3		86.149	2.44	42.9 ± 1	97.88 ± 5.53	15.9 ± 1
	TROVA-7	1333	39.36405	39.16762	4		86.4048	2.432	28 ± 1	105.17 ± 6.05	17.9 ± 1
	TROVA-8	1330	39.36402	39.16765	5		87.2799	2.429	97.3 ± 3	113.39 ± 6.6	15.9 ± 1
	TROVA-9	1333	39.36422	39.16751	5		86.1069	2.405	37.9 ± 2	88.12 ± 4.61	14.4 ± 1
	TROVA-10	1333	39.36417	39.16747	4		87.9176	2.423	18.3 ± 1	72.56 ± 4.37	12.6 ± 1
	TROVA-11	1334	39.36426	39.16739	4		86.5595	2.422	22.9 ± 0	86.49 ± 3.41	14.8 ± 1
	TROVA-12	1330	39.36405	39.16747	4		86.9715	2.424	31.8 ± 1	108.36 ± 4.99	18.2 ± 1
	TROVA-13	1329	39.36404	39.16751	3		88.6287	2.412	31.5 ± 1	99.55 ± 3.68	16.8 ± 1
	TROVA-14	1329	39.364	39.1676	5		90.5756	2.421	23.8 ± 0	75.65 ± 1.99	13 ± 1
	TROVA-15	1330	39.36409	39.16758	4		86.4433	2.35	100.7 ± 1	113.68 ± 4.09	15.8 ± 1
Alluvial fan (NF1)	TROVA-16	1337	39.36606	39.16794	5		86.5954	2.413	23.1 ± 0	117.88 ± 2.89	20.4 ± 1
	TROVA-17	1337	39.36609	39.16787	4		88.6668	2.417	59.2 ± 1	92.72 ± 3.91	14.3 ± 1
	TROVA-18	1342	39.36623	39.16793	5		87.2191	2.425	24.9 ± 0	158.45 ± 3.99	27.5 ± 1
	TROVA-19	1339	39.36624	39.16801	5		85.2149	2.433	16.9 ± 0	121.31 ± 3.57	21.3 ± 1
	TROVA-20	1340	39.36616	39.16807	4		89.6123	2.42	68.9 ± 1	108.48 ± 3.53	16.3 ± 1
	TROVA-21	1334	39.36614	39.16808	5		87.2162	2.429	19 ± 1	92.71 ± 5.32	16.2 ± 1
	TROVA-22	1337	39.36597	39.16805	5		87.5952	2.437	12.7 ± 0	154.71 ± 4.49	27.8 ± 1
	TROVA-23	1338	39.36599	39.16818	5		84.9841	2.397	25.2 ± 0	84.75 ± 2.48	14.5 ± 1
	TROVA-24	1338	39.36614	39.16811	4		87.9378	2.437	20.1 ± 0	90.02 ± 3.64	15.6 ± 1
	TROVA-25	1338	39.3662	39.16811	5		87.999	2.433	72.2 ± 0	212.65 ± 5.35	32.3 ± 2
	TROVA-26	1337	39.36629	39.16782	5		86.4633	2.428	59 ± 1	116.27 ± 3.62	17.9 ± 1
	TROVA-27	1334	39.36632	39.16785	5		85.1503	2.422	37.5 ± 1	112 ± 4.53	18.5 ± 1
	TROVA-28	1334	39.36638	39.16795	5		87.1395	2.404	14.8 ± 0	114.68 ± 4.55	20.3 ± 1
	TROVA-29	1338	39.36631	39.16778	3		87.4031	2.427	41.6 ± 1	95.7 ± 3.08	15.6 ± 1
Strath terrace (T2)	TROVA-DPA-1	1334	39.36423	39.16744	10	45	100.2159	2.422	38.8 ± 1	44.1 ± 3.59	
	TROVA-DPA-2				10	65	103.2174	2.436	39 ± 1	20.3 ± 1.61	
	TROVA-DPA-3				10	95	86.9633	2.356	40.5 ± 1	29.81 ± 2.13	
	TROVA-DPA-4				10	130	102.5455	2.439	42.2 ± 1	42.33 ± 3.26	
	TROVA-DPA-5				10	165	103.3322	2.433	41.1 ± 1	44.28 ± 3.66	
	TROVA-DPA-6				10	205	30.3983	2.407	44.1 ± 1	74.34 ± 6.1	
Alluvial fan (NF1)	TROVA-DPB-1	1337	39.36607	39.168	10	35	101.6746	2.433	38.8 ± 1	40.86 ± 3.57	
	TROVA-DPB-2				10	55	103.4258	2.436	41.7 ± 1	55.26 ± 3.31	
	TROVA-DPB-3				10	85	103.8028	2.428	41.1 ± 1	61.54 ± 3.92	
	TROVA-DPB-4				10	135	74.0231	2.43	42.5 ± 1	91.97 ± 8.29	
	TROVA-DPB-5				10	205	99.8872	2.409	39.1 ± 1	88.85 ± 3.81	

Analytical errors are at 1s level, including the statistical (counting) error and the uncertainty due to normalization of standards and blanks. For details of calculation, please see the methodology section in the supplementary file.

Table 2. Major and trace element data (determined by SGS, Toronto, Canada) of the samples from Köseler site.

Sample name	Mg (wt.%)	Al (wt.%)	P (wt.%)	K (wt.%)	Ca (wt.%)	Ti (wt.%)	Fe (wt.%)	Sm (ppm)	Gd (ppm)	U (ppm)	Th (ppm)
TROVA-1	0.34	0.05	0.01	0.05	39.64	0.01	0.01	0.05	0.05	1.93	0.05
TROVA-2	0.21	0.03	0.01	0.05	39.73	0.01	0.02	0.05	<0.05	0.22	0.05
TROVA-3	0.21	0.02	0.01	0.05	39.75	0.01	0.01	0.05	<0.05	0.92	0.05
TROVA-4	0.27	0.03	0.01	0.05	39.7	0.01	0.01	0.05	0.08	2.91	0.05
TROVA-5	0.27	0.02	0.01	0.05	39.71	0.01	0.01	0.05	0.33	0.51	0.05
TROVA-6	0.4	0.07	0.01	0.05	39.56	0.01	0.05	0.1	0.2	0.25	0.05
TROVA-7	0.39	0.13	0.01	0.05	39.51	0.01	0.06	0.1	0.1	2.77	0.1
TROVA-8	0.55	0.01	0.01	0.05	39.52	0.01	0.02	0.1	0.21	1.48	0.05
TROVA-9	0.19	0.02	0.01	0.05	39.77	0.01	0.01	0.05	<0.05	0.41	0.05
TROVA-10	0.4	0.04	0.01	0.05	39.6	0.01	0.02	0.05	<0.05	0.57	0.05
TROVA-11	0.28	0.03	0.01	0.05	39.7	0.01	0.01	0.05	<0.05	0.45	0.05
TROVA-12	0.35	0.02	0.01	0.05	39.65	0.01	0.01	0.05	0.06	1.05	0.05
TROVA-13	0.64	0.1	0.01	0.05	39.38	0.01	0.05	0.05	0.1	0.16	0.05
TROVA-14	0.25	0.05	0.01	0.05	39.69	0.01	0.03	0.05	0.09	0.38	0.05
TROVA-15	0.22	0.01	0.01	0.05	39.75	0.01	0.01	0.05	0.12	1.22	0.05
TROVA-16	0.33	0.09	0.01	0.05	39.6	0.01	0.03	0.05	0.06	1.36	0.05
TROVA-17	0.28	0.02	0.01	0.05	39.7	0.01	0.01	0.1	0.2	0.69	0.05
TROVA-18	0.43	0.16	0.01	0.1	39.33	0.01	0.08	0.2	0.19	2.22	0.2
TROVA-19	0.25	0.02	0.01	0.05	39.72	0.01	0.01	0.05	<0.05	0.49	0.05
TROVA-20	0.44	0.04	0.01	0.05	39.58	0.01	0.01	0.05	0.05	0.77	0.05
TROVA-21	0.2	0.04	0.02	0.05	39.72	0.01	0.03	0.05	0.06	4.66	0.05
TROVA-22	0.19	0.03	0.01	0.05	39.75	0.01	0.01	0.05	0.06	2.55	0.05
TROVA-23	0.41	0.3	0.01	0.2	38.99	0.02	0.09	0.3	0.28	3.15	0.4
TROVA-24	0.36	0.04	0.02	0.05	39.45	0.01	0.02	0.2	0.15	0.79	0.05
TROVA-25	0.67	0.01	0.01	0.05	39.44	0.01	0.02	0.05	0.11	1.11	0.05
TROVA-26	0.19	0.05	0.01	0.05	39.72	0.01	0.03	0.05	<0.05	1.77	0.05
TROVA-27	0.14	0.05	0.01	0.05	39.77	0.01	0.02	0.1	0.2	1.26	0.05
TROVA-28	0.21	0.03	0.01	0.05	39.74	0.01	0.01	0.05	0.06	2.38	0.05
TROVA-29	0.93	0.05	0.02	0.05	39.22	0.01	0.03	0.05	<0.05	0.93	0.05
TROVA-DPA-1	0.26	0.05	0.01	0.05	39.67	0.01	0.04	0.1	0.18	0.96	0.05
TROVA-DPA-2	0.31	0.49	0.01	0.2	38.79	0.02	0.3	0.5	0.65	1.03	0.5
TROVA-DPA-3	0.28	0.31	0.01	0.1	39.23	0.01	0.23	0.4	0.49	1	0.5
TROVA-DPA-4	0.28	0.25	0.03	0.1	39.26	0.01	0.21	0.4	0.48	1	0.4
TROVA-DPA-5	0.31	0.38	0.02	0.1	39.1	0.02	0.29	0.4	0.54	1.04	0.5
TROVA-DPA-6	0.28	0.18	0.01	0.05	39.46	0.01	0.2	0.3	0.44	0.94	0.4
TROVA-DPB-1	0.24	0.07	0.02	0.05	39.64	0.01	0.07	0.2	0.19	0.89	0.2
TROVA-DPB-2	0.26	0.05	0.01	0.05	39.66	0.01	0.06	0.1	0.21	0.91	0.1
TROVA-DPB-3	0.24	0.07	0.02	0.05	39.63	0.01	0.09	0.2	0.19	0.84	0.1
TROVA-DPB-4	0.22	0.05	0.01	0.05	39.68	0.01	0.07	0.1	0.21	0.81	0.05
TROVA-DPB-5	0.23	0.06	0.01	0.05	39.67	0.01	0.06	0.1	0.2	0.88	0.05

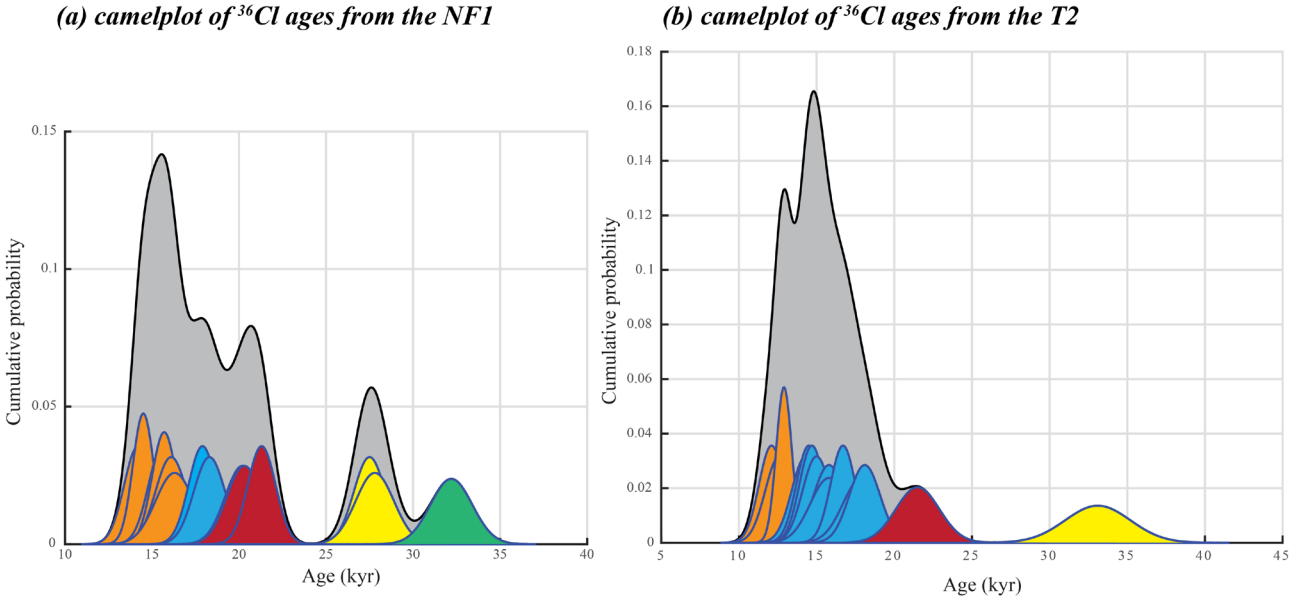

Figure 10. Camelplot diagrams of ^{36}Cl surface exposure ages for **(a)** NF1 alluvial fan and **(b)** T2 terrace surfaces. Gaussian probability distribution functions (black) were calculated by using MATLAB-based program Camelplot (G. Balco, http://depts.washington.edu/cosmolab/pubs/gb_pubs/camelplot.m). Probability values are normalized to have a unit area for each individual probability distribution. Shaded areas indicate the sum of the probability distributions for all samples. The sum of the probability distributions makes four major and one minor peaks in case of NF1, showing a total of four sets of ages, whereas we observe four sets of ages in T2. Samples of the same set are painted with the same colour. Both NF1 and T2 are undisturbed surfaces without any sign of significant vertical erosion; therefore, we suggest that the youngest exposure ages, orange coloured curves, represent both surfaces.

rates, attenuation length, rock density, topographic shielding, and erosion rate, as explained above in detail. The variation of modelled concentrations against depth is plotted in Figure 11.

Cosmogenic ^{36}Cl dates are modelled with boxcar probability in all of our slip-rate calculations, indicating that any age within the range t_1 and t_2 is equally probable, and no age beyond this range is possible in the calculation of probability density functions (pdfs) of ages by using the computer program written by Zechar and Frankel (2009).

4. Slip-rate of the Ovacık Fault

4.1. Köseler Site and local geomorphology

The OF is clearly exposed on fan surfaces and across the margins between fans and their incised channels. Unfortunately, the offset terrace risers are only preserved on the Kuru Dere alluvial fan, whereas others have been eroded by fluvial lateral erosion (Çaşırlık Deresi) or anthropogenic activity (Aksu Deresi) (Figure 3). The geomorphology of our slip-rate site, Köseler, is mainly shaped by the widely distributed Kuru Dere alluvial fan (NF1), its radial distribution channels (NF1') and inset terrace surfaces (T1 and T2) (Figures 3 and 4). Not only the shaded DEM map (Figures 4 and 7) but also linear ('cross') or semicircular topographic ('arc') profiles clearly represent the interrelationship of these surfaces (Figure 6). Cross profile 1-1' shows a typical plano-convex shape of an alluvial fan (Blair and McPherson, 1994), while both arc profiles 2-2' and 3-3' display an uneven concave geometry that might be shaped by the remnants of an old alluvial lobe or debris cover at the eastern and western margins (Figure 6). This probable older fan and NF1 started to form after the retreat of late Pleistocene glaciers in the Karagöl Valley, which were later followed by the incision of the south flowing stream (Kuru Dere) into the alluvial fan deposits and led to the formation of two terrace levels, T1 and T2. The relatively older T2 is a single-paired strath terrace, which is only seen at the western flank of Kuru Dere, whereas T1 represents the modern channel deposits. NF1, NF1', T2, and T1 are clearly marked on fault-parallel profiles (Figures 6d and e).

The OF is mainly characterized with an obvious fault scarp on the Kuru Dere alluvial fan (Figures 3 and 4). This scarp is accommodated with slip-rate pull-aparts or local uplifts, related to its geometric discontinuities along its course. We also observe uplifted and downthrown terrains in larger scale, where this sinistral strike-slip fault makes restraining or releasing bends/step-overs (Figure 4). The restraining step-over to the west of the Kuru Dere Fan is marked with a series of linear ridges at Koyungölü Village (Figure 3). These parallel/subparallel structures and their faulted margins suggest evidence for two successive step-

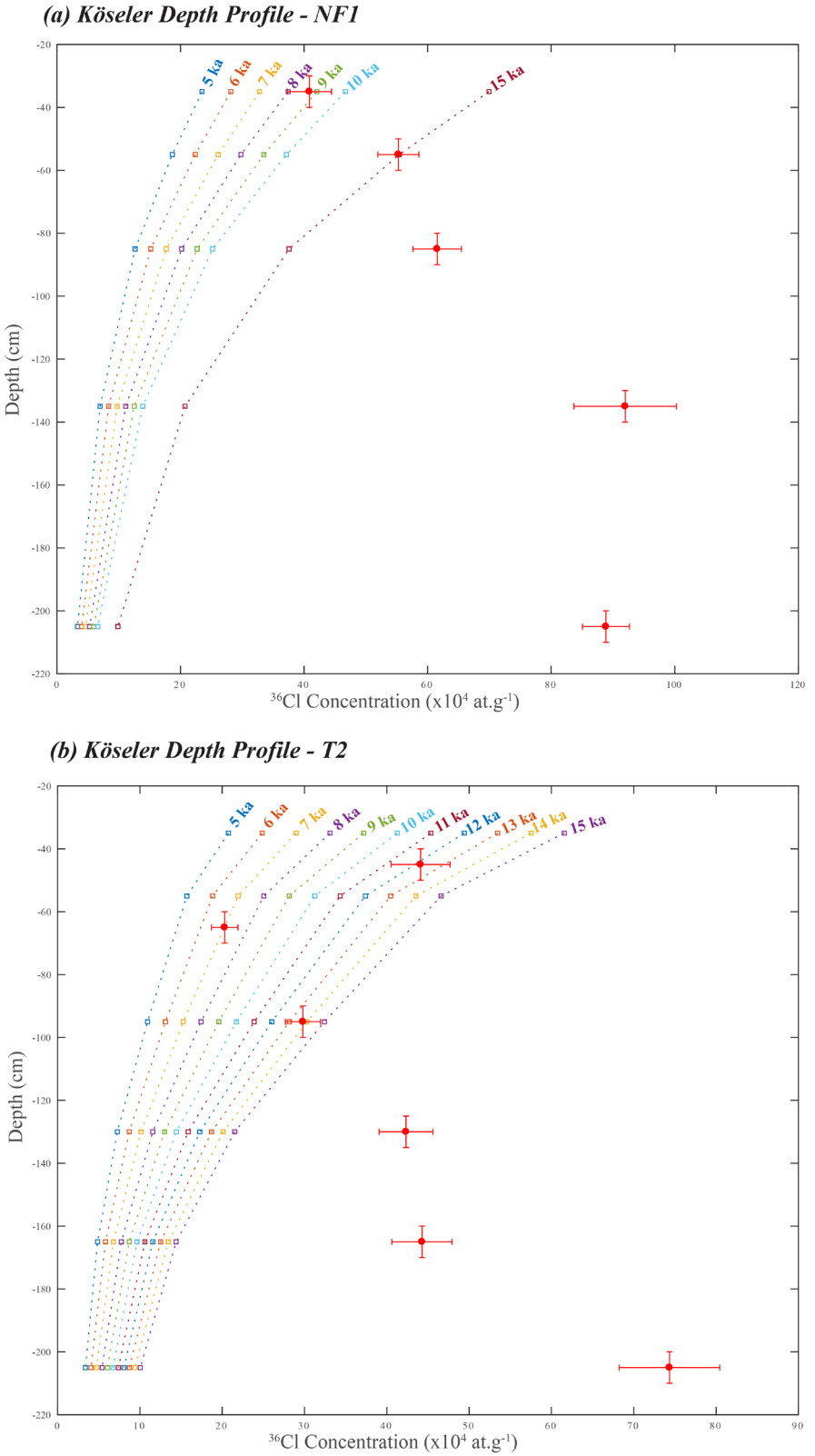

Figure 11. Measured cosmogenic ^{36}Cl concentrations from the **(a)** NF1 and **(b)** T2 surfaces of the Köseler Site against depth. 1σ uncertainties in concentrations and uncertainties in depth are shown by vertical and horizontal error bars. The variation of modelled cosmogenic ^{36}Cl concentrations for hypothetical exposure times against depth is indicated with different colours.

overs, which are separated of about 350 m between each other (Figure 4b). In the eastern margin, the OF makes a 30° of releasing bend, that is clearly marked with the downthrown of the southern block to the north of the Paşadüzü Village (Figures 3 and 4c). Beside the vertical component of sinistral shear accompanied by these geometric discontinuities, the OF does not show any clear evidence of vertical slip (Figures 6f and 6g). The horizontal slip is clearly observed across the margins of the alluvial fan (NF1), its subplanar fan surface (NF1'), and the oldest terrace (T2) of the incised channel, which we discuss in detail below. Another active channel to the east of the Kuru Dere alluvial fan display the most distinct and remarkable sinistral deflection of about 150 to 280 m (Figures 3 and 4). However, arc profiles 2-2' and 3-3' exhibit that this channel follows the topographic boundary along the NF1' eastern margin and the vertical offset due to the local releasing bend (dark blue arrows in Figures 6b and 6c); thus, any related offset analysis on this deflection would be an overestimation of slip and deceptive for the activity of the OF in the Ovacık Basin.

4.2. Offset features of the Köseler Site

We identified and mapped two offsets between the margins of the Kuru Dere alluvial fan (NF1), subplanar fan surface (NF1') and the strath terrace (T2) of the incised active channel near the Köseler Village (39.3643°N, 39.1688°E; Figures 3, 4, and 7).

Among these two markers, the NF1/T2 riser offset is spectacular not only because of its sharp displaced geometry but also because of being insulated from lateral erosion. This geomorphological feature is separated from the active channel with the T2 terrace surface (Figure 7). The riser's trend is almost perpendicular to the OF and does not include any curves or bends close to the deformation zone. The LaDiCaoz solution yields 17 m of optimal sinistral displacement based on the preslip topography reconstruction (Figure 8a). Moreover, incremental slip restorations suggest a best solution between 15 and 22 m (Figure 8b). This total amount of slip is far exceeded by the approximately 100-m-width of the modern channel (Figure 7).

The western lobe of the Kuru Dere alluvial fan includes multiple imprints of abandoned distributary channels that have a distinct radial pattern (Figure 4). Hereby, risers separating fan surface (NF1) and subplanar fan surfaces (NF1') of distributary channels, are mostly controlled by lateral erosion due to a negative westerly slope (Figure 6d). The NF1/NF1' riser, which is about 450 m away from the modern channel edge, displays a sinistral offset across the

fault (Figure 7). The optimal preslip topographic reconstruction of fault-parallel profiles suggest 21 m of sinistral offset, whereas incremental slip analyses yield a best solution between 19 and 24 m (Figure 9). has a straight geometry and shows no deflection or bending.

4.3. Chronology of offset features at the Köseler Site

The NF1 and T2 surfaces are characterized by partly buried coarse cobbles, which are derived from the Triassic to Cretaceous limestones of the Munzur Mountains to the north. These cobbles are mostly rounded/well-rounded and spherical, and their surfaces show no evidence of weathering. We sampled twenty-nine coarse cobbles from the best-preserved locations of the T2 and NF1 for the cosmogenic 36Cl surface exposure geochronology. Moreover, two trenches were excavated down to approximately 2 m in both surfaces to take sandsize sediment samples from the matrix of the gravels for depth profiling (Figure 5 and Table 1).

The analyses of fifteen surface cobble samples from T2 give a very wide range of ages from 12.2 ± 0.8 ka to 33.3 ± 2.2 ka. Fourteen cobble samples from NF1 also provide a similar distribution between 14.3 ± 0.8 ka to 32.3 ± 0.8 ka (Table 1). The probability distributions of these samples provide five and four age clusters for NF1 and T2, respectively (Figure 10). We interpret the youngest clusters to represent the abandonment age of these unmodified and uneroded surfaces, while all older ages are the result of inheritance on both surfaces. The fact that the age of the strath terrace cannot be older than the alluvial fan in the Köseler Site also supports our interpretation. Therefore, five dating results from NF1, varying between 14.3 ± 0.8 and 16.3 ± 0.8 ka, and three ages from T2, varying between 12.2 ± 0.8 and 13.0 ± 0.5 ka, of the youngest clusters are accepted to provide the most probable temporal control on these morphological features by using only the surface samples (Figure 10).

On the other hand, ^{36}Cl concentrations of depth profile samples do not decrease exponentially with depth in NF1 and T2 surfaces. In case of NF1, we observe a pattern in which almost all concentrations increase with depth. In T2, we see a similar pattern except that only one sediment sample at depth of 65 cm from the surface show a lower concentration than the upper sample (Table 1 and Figure 11). These measured ^{36}Cl concentrations suggest that both surfaces are dominated by multiphase sediment fluxes from the source and most of the samples already had ^{36}Cl when they were deposited; thus, we used a similar approach to 'profile rejuvenation methodology' of Le Dortz et al. (2012). This method relies on the simple hypothesis that at least one of the depth-profile samples would be emplaced with no or negligible inherited component and on the obvious principle that none of the analysed sample has been emplaced with a negative cosmogenic nuclide concentration. In order to give the upper age boundary to each surface with these assumptions, we first calculated theoretical cosmogenic ^{36}Cl concentrations for exposure times between 5 ka and 15 ka with 1 ka incremental steps

by using the same chemical compositions and depths of each sample and the method of calculation provided by Alfimov and Ivy-Ochs (2009). Then, we picked the lowest concentrations of the measured samples, which are thought to include the minimum inheritance, and correlated them with these calculated theoretical values (Figure 11). Finally, measured cosmogenic ^{36}Cl concentrations of the samples at 35 cm depth from NF1 and 65 cm depth from T2 suggest that the most probable maximum ages for NF1 and T2 are 8–10 ka and 6–8 ka, respectively.

5. Slip-rate estimates: interpretation of offsets and chronology

As it is described in detail above, we measured two offset reference margins, NF1/T2 and NF1/NF1' risers at the Köseler Site. In the calculation of probability distributions for each offset margins, we included trapezoid uncertainties to the upper and lower offset limits (trapezoid uncertainty column in Table 3). Both NF1 and T2 surfaces were dated to calculate the slip-rate of the OF. The upper tread model defines a maximum age for a riser, whereas the lower tread provides a minimum age on the assumption that the riser cannot be older than the age of the upper surface or it cannot be younger than the age of the lower bounding surface. Therefore, in all circumstances, the usage of the upper tread's age represents the minimum rate, while the lower tread's age provides the maximum slip-rate for terrace risers. We made separate calculations by using the ages of (a) the upper tread for minimum slip rate, (b) the lower tread for maximum slip rate, or (c) both of them for an intermediate solution. All of the slip-rate results are reported with 2s errors (Table 3 and Figures 12 and 13).

We used the cosmogenic ^{36}Cl ages of NF1 surface and applied only upper–tread reconstruction in slip-rate calculations for the NF1/NF1' offset. Surface ages of the youngest cluster (TROVA–17, –20, –21, –23, –24, and –29) together with the total slip of this margin yield a minimum slip-rate of 1.4 +0.3/–0.3 mm/a. On the other hand, the much younger modelled age of 8–10 ka from the depth profile on NF1 suggests a faster rate of 2.4 +0.5/–0.4 mm/a (Table 3 and Figures 12 and 13).

For NF1/T2 offset, where we have temporal control from all bounding surfaces, we calculated slip rates by using the ages of the upper surface (upper tread model), the ages of the lower surface (lower tread model), or ages of both surfaces (intermediate solution). The cumulative offset of 15 to 22 m together with the surface exposure ages of NF1, T2, or of both surfaces yield slip rates of 1.2 +0.4/–0.3 mm/a, 1.5 +0.4/–0.3 mm/a and 1.3 +0.5/–0.4 mm/a for upper tread, lower tread and intermediate solution models, respectively. On the other hand, modelled depth profile ages 8–10 ka of NF1 and 6–8 ka of T2 suggest faster upper tread, lower tread, or intermediate solution rates of 2.1 +0.6/–0.5 mm/a, 2.8 +0.7/–0.7 mm/a or 2.3 +1.1/–0.7 mm/a.

In order to reduce the uncertainty, we analysed the accurate end-member reconstructions where any of Cowgill's (2007) six geomorphic indices, (a) riser offset versus inset channel width/offset, (b) offset of primary features versus riser, (c) scarp morphology, (d) deflected riser geometry, (e) diachronous tread abandonment, and (f) parallel slip vectors link surface to date, can be applied.

Table 3. Slip-rate estimates, calculated with probability distributions of each offset feature and their ages in consideration of three different scenarios, the upper tread reconstruction, the intermediate solution, and the lower tread reconstruction.

Age model	Offset feature	Dated unit	Displacement (m)[i]		Trapezoid unc. (m)	Date (ka)[ii]		Model	Slip rate (mm/a)[iii]
			Dmin	Dmax		Amin	Amax		
(a) Surface ages	NF1/T2	NF1	15	22	+1/–1	13.5	17.3	Upper	1.2 +0.4/–0.3
	NF1/T2	NF1 and T2	15	22	+1/–1	11.4	17.3	Intermediate	1.3 +0.5/–0.4
	NF1/T2	T2	15	22	+1/–1	11.4	13.5	Lower	1.5 +0.4/–0.3
	NF1/NF1'	NF1	19	24	+1/–1	13.5	17.3	Upper	1.4 +0.3/–0.3
(b) Depth profile	NF1/T2	NF1	15	22	+1/–1	8	10	Upper	2.1 +0.6/–0.5
	NF1/T2	NF1 and T2	15	22	+1/–1	6	10	Intermediate	2.3 +1.1/–0.7
	NF1/T2	T2	15	22	+1/–1	6	8	Lower	2.8 +0.7/–0.7
	NF1/NF1'	NF1	19	24	+1/–1	8	10	Upper	2.4 +0.5/–0.4

[i] *Upper and lower boundaries of offset measurements.*
[ii] *Upper and lower age limits are determined by combination of all available ^{36}Cl ages from surface samples and model ages based on the lowest ^{36}Cl concentration of depth profiles.*
[iii] *Slip rates (2σ) are calculated with the boxcar and the trapezoid approaches of Zechar and Frankel [2009] for age and offset measurements, respectively.*

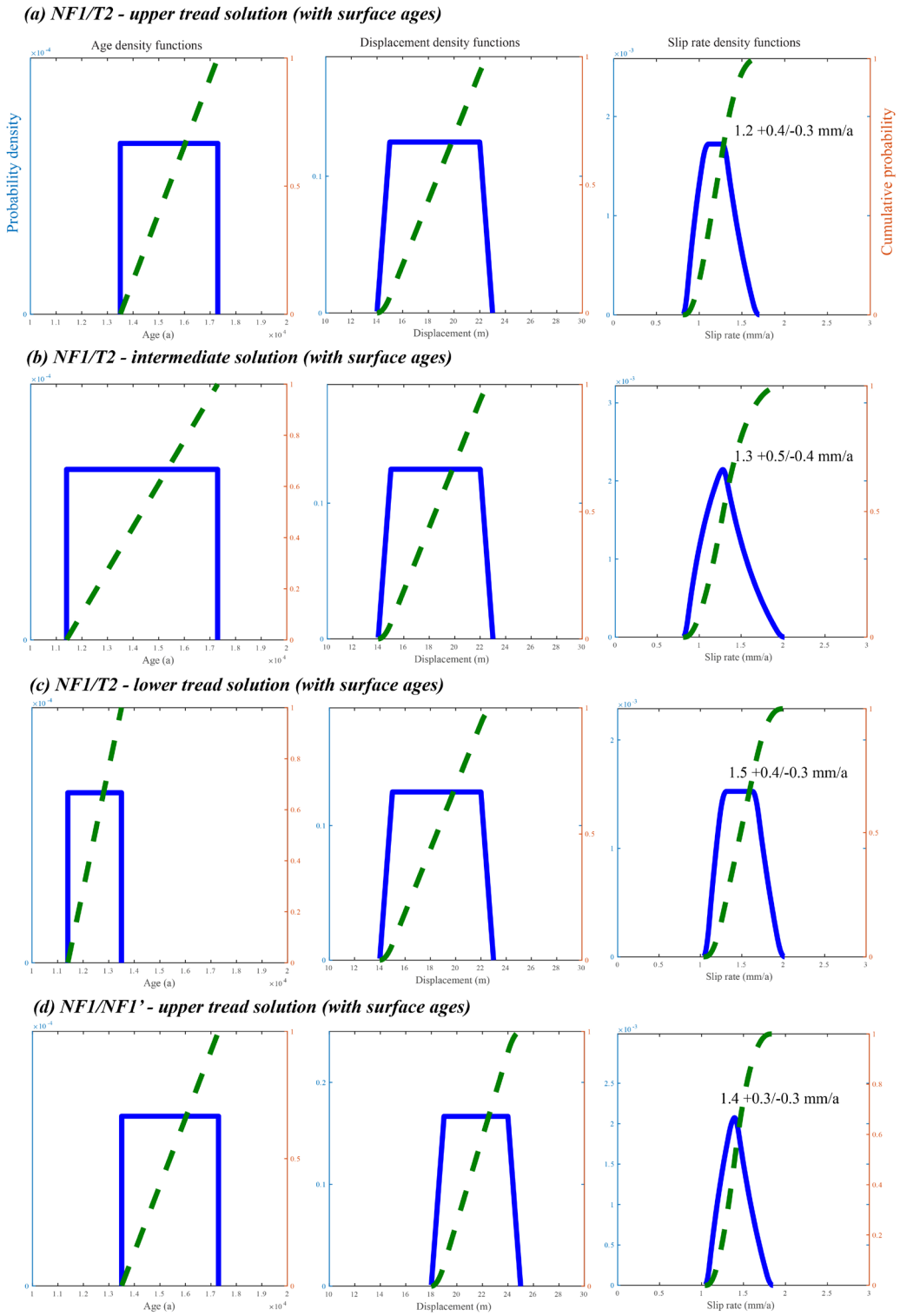

Figure 13. Probability distribution functions (pdf) to calculate slip rates for two different offset risers, NF1/T2 and NF1/NF1', and model ages from ^{36}Cl depth profiles at the Köseler Site. Boxcar and trapezoid approaches of Zechar and Frankel (2009) are used in calculation of age and offset probability distributions, respectively. The blue solid lines are probability densities, whereas green dashed lines indicate cumulative probabilities. We used **(a)** the NF1/T2 riser offset with ages of the upper tread, **(b)** the NF1/T2 riser offset with ages of both and lower and upper treads, **(c)** the NF1/T2 riser offset with ages of lower tread, and **(d)** the NF1/NF1' riser offset with ages of upper tread.

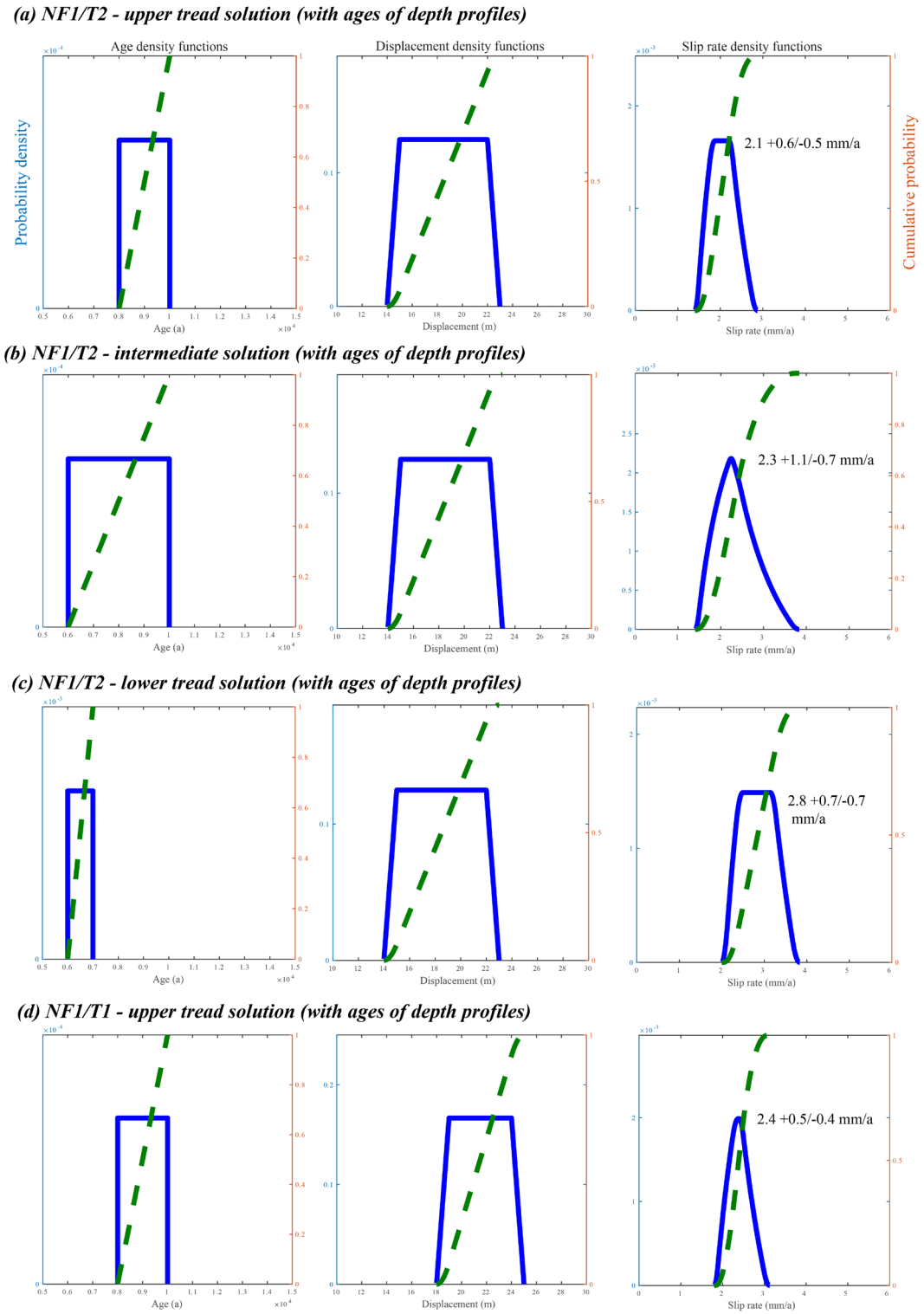

Figure 12. Probability distribution functions (pdf) to calculate slip rates for two different offset risers, NF1/T2 and NF1/NF1', and ^{36}Cl surface exposure ages at the Köseler Site. Boxcar and trapezoid approaches of Zechar and Frankel (2009) are used in calculation of age and offset probability distributions, respectively. The blue solid lines are probability densities, whereas green dashed lines indicate cumulative probabilities. We used **(a)** the NF1/T2 riser offset with ages of the upper tread, **(b)** the NF1/T2 riser offset with ages of both and lower and upper treads, **(c)** the NF1/T2 riser offset with ages of lower tread, and **(d)** the NF1/NF1' riser offset with ages of upper tread.

In case of NF1/NF1', the limited age control restrains us to calculate only the minimum slip rate. For NF1/T2, only two of these indices, riser offset versus inset channel width/offset and deflected riser geometry can be applied. Since the NF1/T2 offset is highly exceeded by the width of the inset channel and there is no bending (deflected geometry) on the general trend of this riser, we strongly suggest that all displacement, which happened before the abandonment of T2, has been totally eroded and the slip was only started to be recorded after the abandonment of its lower tread. Thus, 1.5 +0.4/–0.3 mm/a or 2.8 +0.7/–0.7 mm/a geologic rates of lower-tread reconstruction, which were calculated by using surface exposure ages or modelled depth profile ages, respectively, represent the strain accumulation after the abandonment of the T2 strath terrace at the Köseler Site.

6. Discussion

6.1. Surface exposure ages vs modelled depth profile ages: implications for slip-rate calculations for the Köseler Site

The analyses of displayed landforms at the Köseler Site result in two offset measurements, 15–22 m and 19–24 m, across terrace risers NF1/T2 and NF1/N1', respectively. Both NF1/T2 and NF1/NF1' represent a sharp sinistral displacement along the OF (Figures 7–9). We have age control from both neighbouring surfaces to the NF1/T2, whereas the age of NF1/NF1' is limited only from the upper surface.

In terms of temporal control on these two independent offset features, surface exposure ages and depth profiling yield incompatible dates both for the formation of the alluvial fan and inset terrace at the Köseler Site. Cosmogenic ^{36}Cl surface exposure ages yield 13 to 18 ka for NF1 and 11 to 14 ka for T2. However, the nonexponential distribution ^{36}Cl concentrations in the depth-profiles suggests that the amount of the accumulated cosmogenic ^{36}Cl after deposition is less than the existing cosmogenic ^{36}Cl during the time of deposition, i.e. inheritance, which is also supported with the multimodal distribution of surface exposure ages. The glacier oscillations around 18 ka and 14 ka (Yeşilyurt et al., 2015) should also have been long after replaced by fluvial deposition at the northern margin of the Ovacık Basin. Thus, we consider that depth-profile samples already had accumulation of ^{36}Cl concentrations. We follow a similar approach to 'profile rejuvenation method' of Le Dortz et al. (2012) and calculate independent exposure ages from our depth-profile concentrations, which has been applied for similar cases in different sedimentary environments (cf. Perouse et al., 2017; Stange et al., 2013; Viveen et al., 2012). The profile rejuvenation method simply based on basic assumptions such as (a) insignificant post depositional erosion, (b) relatively short and continuous aggradation, (c) sediment supply from the same source, and (d) that at least one sample of the depth-profile was emplaced with no inherited terrestrial cosmogenic nuclide component (Le Dortz et al., 2012; Stange et al., 2013). Briefly, we accepted only the lowest measured concentration with the assumption that the measured concentration would either result from *in-situ* production or have minimum amount of inheritance, thus, the maximum abandonment age of the alluvial fan or the inset terrace surface corresponds to the time needed for the depth-profile sample, which could be brought back from its measured concentration to a null concentration without bringing other depth-profile samples to a negative concentration. The calculated model ages from depth profiles for the same chemical composition and depth of each sample suggest much younger ages, 8–10 ka and 6–8 ka, for NF1 and T2, respectively.

We used the surface exposure and modelled depth-profile ages together in our slip-rate calculations and reported our results separately for both cases (Table 3). Naturally, slip-rate estimates in preferred scenarios of lower-tread reconstruction for NF1/T2 and upper-tread reconstruction for NF1/NF1' with surface exposure ages are highly exceeded by almost a factor of two with rates that were calculated with depth-profile ages. Considering the evidence of inheritance and the evidence for glacial activity until 14 ka (Yeşilyurt et al., 2015), we prefer to use the modelled depth-profiles ages and suggest slip rates of 2.8 +0.7/–0.7 mm/a (NF1/T2, lower-tread reconstruction) and 2.4 +0.5/–0.4 mm/a (NF1/NF1', upper-tread reconstruction) for the Holocene behaviour of the OF at the Köseler Site.

6.2. Slip-rate estimates on the active structures of Anatolia

There are a limited number of morphochronology-based slip-rate estimates along the active structures of the central Anatolian *Scholle* (Figure 14 and Table 4). Most of these studies are concentrated on the Central Anatolian Fault Zone (CAFZ), while there is a single very long-term slip-rate estimate for the Malatya Fault. This study adds the morphochronology-based slip-rate result obtained throughout the OF to the existing knowledge.

Two closely spaced studies provide conflicting slip-rate estimates for the southern segments of the CAFZ. Sarıkaya et al. (2015) calculate 4.2 ± 1.9 mm/a horizontal rate for a time period between 104.2 ± 6.5 ka and 64.5 ± 5.6 ka at the Yalak River Site and propose that there have not been any surface rupturing earthquakes since 64.5 ± 5.6 ka on this fault strand. However, Higgins et al. (2015) claim that morphological surfaces at the Yalak River Site has been subjected to reworking by erosion; thus, another but nearby location, the Martı River Site exhibit a more reliable slip rate, 1.1 ± 0.4 mm/a (erosion corrected) or 1.2 ± 0.4 mm/a (erosion and inheritance corrected), as an average

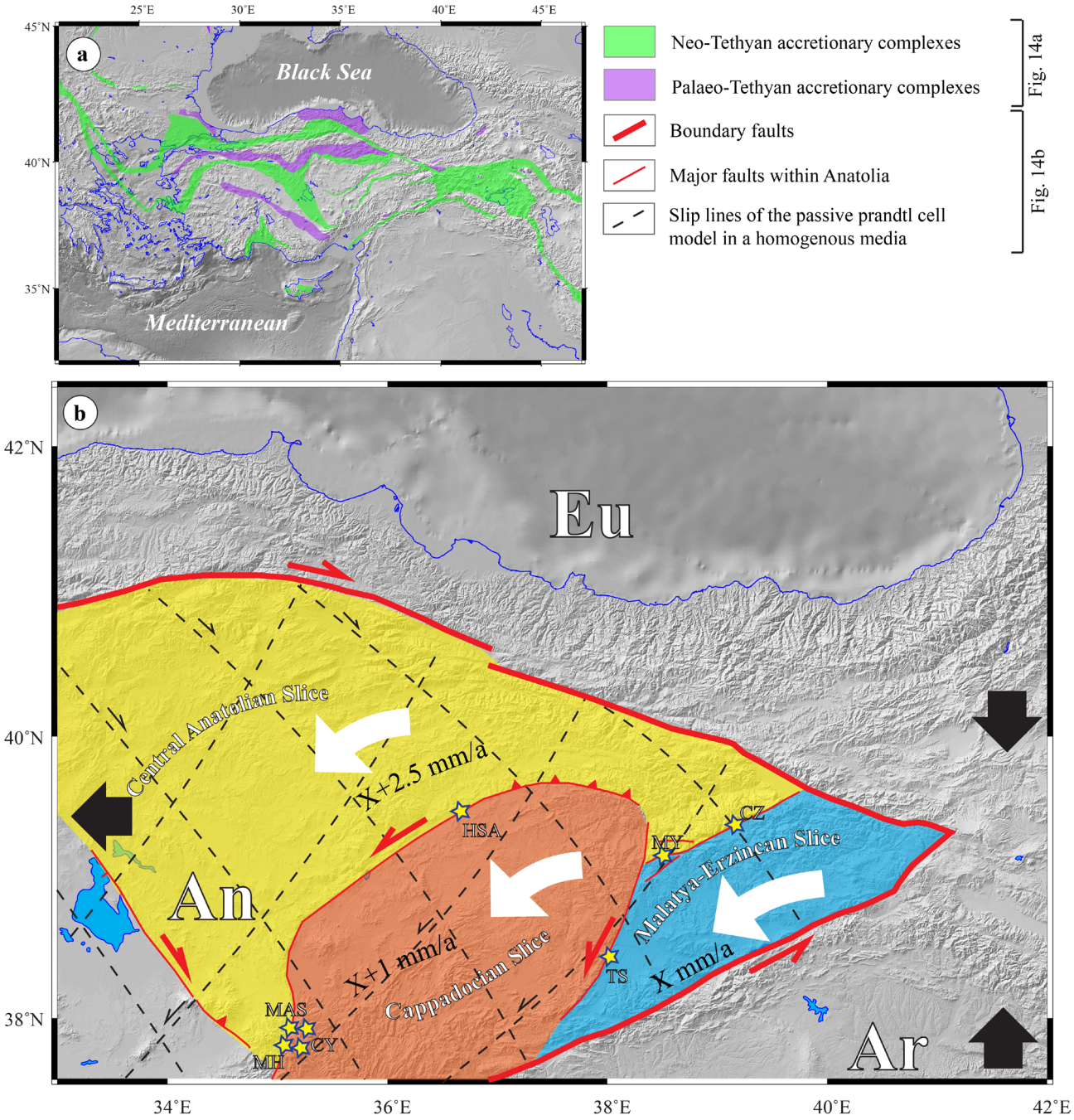

Figure 14. (a) The map showing the distribution of Tethyan accretionary complexes within and around Anatolia (modified after Şengör et al. (2019b)), **(b)** Comparison of slip lines of the theoretical passive Prandtl cell model (dashed lines) and tectonic slices with secondary faults making their boundaries. White arrows show the relative motion of slices with respect to Arabia, whereas black arrows represent the convergence between Eu and Ar, and the westward extrusion of material towards west between boundary elements, the NASZ and EASZ. Yellow stars mark the location of geological or palaeoseismological slip-rate sites (For details please see Table 4). Key to lettering: Eu, Eurasia; Ar, Arabia.

value for the last approximately 60 ka. We agree that there is no visible sinistral slip between the boundaries of inset terraces at the Yalak River Site. Nevertheless, the deflected geometry of the riser between the alluvial fan and the neighbouring inset terrace (the boundary between Y1 and Y3 in figures 2 and 5 in Sarıkaya et al. (2015)) and limited spatial distribution of inset terraces (e.g., Y3 is partly preserved on a very limited area on the east/southeastern

Table 4. Geological slip-rate estimates along the Ovacık and other strike-slip faults of the Central 'Ova' Province.

Fault	Site	LON (°E)	LAT (°N)	Evidence	Slip	Age	Slip rate	Reference
Ovacık Fault	Karasu River	38.65	39.2	Age of offset river	14 km	~5.3 Ma	~2.7 mm/a	MY - Yazıcı et al. (2021)
Ovacık Fault	Köseler	39.17	39.4	Morphchronology of fan and terraces	15–22 m	6-8 ka	2.8 ± 0.7 m/a	CZ - This study
Malatya Fault	Tohma River	38.07	38.5	Morphochronology of offset terraces	1.4–1.5 km	1.4 Ma	1.0–1.12 mm/a	TS - Sançar et al. (2020)
Central Anatolian Fault Zone	Tecer	36.93	39.4	Reccurence of palaeoseismic events	-	last 10 ka	~1 mm/a	HSA - Akyüz et al. (2012)
Central Anatolian Fault Zone	Martı River	35.07	37.8	Morphochronology of offset terraces	69 ± 5 m	52 ± 12 to 61±14 ka	1.1 ± 0.4 mm/a	MH - Higgins et al. (2015)
Central Anatolian Fault Zone	Yalak River	35.09	37.8	Morphochronology of offset terraces	168 ± 2 m	104.2 ± 16.5 to 64.5 ± 5.6 ka	4.2 ± 1.9 mm/a	MAS - Sarıkaya et al. (2015)
Central Anatolian Fault Zone	Cevizli Fault	35.12	37.8	Morphochronology of offset morrain and talus	13.1 ± 1.4 m (vertical)	21.9 ± 1.8 ka	0.66 ± 0.12 mm/a (vertical)	CY - Yıldırım et al. (2016)
Central Anatolian Fault Zone	Kartal Fault	35.1	37.9	Morphochronology of offset alluvial fan	120 ± 10 m (vertical)	104.2 ± 16.5 ka	1.15 ± 0.21 mm/a (vertical)	CY - Yıldırım et al. (2016)

block of the fault) suggest incomplete lateral erosion and scarp degradation most probably due to the dip slip component of the deformation. We suggest that the total deflection of the Yalak River system should have happened after the abandonment of the alluvial fan (Y1) considering the evidence for lateral erosion. In this case, the 168 ± 2 m offset of the Yalak River, and the 104.2 ± 6.5 ka age of the alluvial fan together yield a horizontal slip-rate of 1.6 ± 0.1 mm/a (2s). Further to the north/northeast, the horizontal slip-rate is suggested to be about 1 mm/a by using the interevent time between two palaeoseismic events, revealed in the Tecer Segment of the CAFZ (Akyüz et al., 2012). The horizontal elastic block model slip-rate of about 1 mm/a for the CAFZ (Aktuğ et al., 2013b) supports the estimate of Akyüz et al. (2012), but it is slightly exceeded by all other morphochronology-based studies. Furthermore, the vertical rates of this geodetic study suggest extensional component, which is documented along the normal faults parallel/subparallel to the southern segments of the CAFZ (Yıldırım et al., 2016).

Although the MF and OF together is thought to be parts of the same fault system, the MOFZ, they exhibit differential deformation rates. The offset of Tohma River and related morphological features suggest a maximum geological slip-rate of 1.12 ± 0.01 mm/a as an average value since 1.4 Ma for the MF (Sançar et al., 2020). This very long-term deformation rate is supported by the mean palaeoseismic interevent time of 2275 ± 605 years for the MF's northern segments (Sançar et al., 2019). Even though a similar average interevent time, 2400 ± 765 years, is revealed for the OF (Yazıcı et al., 2021), it represents only a portion of total deformation, which is distributed among multiple parallel/subparallel fault strands of a wide shear zone at the western OF. The distributed deformation is supported by the multisegment deflection of the Karasu River, which yield a very long-term slip-rate of about 2.7 mm/a since the early Pliocene (Yazıcı et al., 2021), almost identical to our morphochronology-based estimates. These rates are significantly faster than GNSS-based elastic block model rates of 1.2 ± 0.3 mm/a (Aktuğ et al., 2013a) or 1.8 ± 0.1 mm/a (Aktuğ et al., 2013b) for the same section of the fault system. Moreover, there is no clear evidence for vertical motion, except some local features due to the releasing or restraining bending/step-overs (Figures 4a and 4b) within the Ovacık Basin, in contrast to block-model results, which suggest normal component of slip. Further to the west/southwest along the OF, the structural data (Kaymakçı et al., 2006) and the uplifted morphology (Yazıcı et al., 2018) together show reverse (compressional) but not a normal (extensional) component of motion in addition to the sinistral strike-slip deformation.

6.3. Implications for the internal deformation of Anatolia

Although the main boundary elements, the NASZ and EASZ, were thought to be responsible for sharing almost all deformation during the westward extrusion of the Anatolia, our slip-rate estimates and recent multidisciplinary studies (e.g., Özener et al., 2010; Aktuğ et al., 2013a; Aktuğ et al., 2013b; Yıldırım, 2014; Higgins et al., 2015; Sarıkaya et al., 2015; Sançar et al., 2019; Acarel et al., 2019; Yıldırım et al., 2016; Yazıcı et al., 2018; Sançar et al., 2020; Yazıcı et al., 2021; Özbey et al., 2022) show that there is remarkable internal deformation within this continental piece. The MOFZ is only one of the strike-slip faults of many others, which partly share the total internal strain. The NE-striking faults (e.g., Central Anatolian Fault Zone—CAFZ) are parallel/subparallel to the MOFZ with a sinistral strike-slip component of motion (Figures 1a and 1b), whereas NW-striking structures (Tuzgölü Fault Zone and other small-scale faults, such as Salanda, Akpınar and Delice faults are mainly dominated by dextral strike-slip component of motion (see Bozkurt, 2001 for review of these structures). Not only the geomorphic indices document the morphological response to the tectonic activity of these faults (e.g., Yıldırım, 2014; Yazıcı et al., 2018), but also the geological slip-rate estimates (e.g., Higgins et al., 2015; Sarıkaya et al., 2015; Yıldırım et al., 2016; Sançar et al. 2020) and widely distributed GNSS measurements and their analyses (Aktuğ et al., 2013a; Aktuğ et al., 2013b; Özener et al., 2010; Özbey et al., 2022) provide evidence for the internal deformation within Anatolia.

One of the first hypotheses to explain the internal deformation and related structures is suggested by Şengör (1979), who correlates the slip lines of the active Prandtl cell model and internal faults of Anatolia (figure 6 in Şengör (1979)). Gürsoy et al. (1997) follows the hypothesis on the Prandtl cell model to explain the counterclockwise rotation of blocks within Anatolia. In later studies, Anatolia is suggested to be deformed by integrated processes of slab break-off and Hellenic trench retreat especially along its southern parts (e.g., Barka and Reilinger, 1997; Schildgen et al., 2012; Schildgen et al. 2014) or dripping of the thickening lithosphere (Göğüş et al., 2017), all of which claim to explain the uplift and vulcanicity but do not refer to the observed strike-slip deformation except Barka and Reilinger (1997). These strike-slip faults are thought to be secondary shallow structures, limited to the upper crust (Higgins et al., 2015), slicing the 'rigid' Anatolia (Barka and Reilinger, 1997; Higgins et al. 2015). The resultant slices rotate in an overlapping fashion, where the shortening will be distributed to gentler structures (Şengör et al., 2019a) such as Sarıkız, Gürün, and Ayvalı faults (Emre et al., 2013).

Although the general trends of strike-slip faults of internal Anatolia are similar to the 'exponential curve' shapes and orientations of slip-lines of an active Prandtl cell

model, the sense of motion along these faults corresponds to the compressional passive Prandtl cell model (dashed lines in Figure 14b) of Varnes (1962), where the boundary elements move toward each other and the material between them moves away from the apex of the wedge (Sançar et al., 2018). The misfit between the orientation of slip lines in the passive Prandtl cell model and the observed structural members of the Anatolia's interior can occur due to (a) the velocity difference of a factor of about two between the boundary faults, the NASZ and the EASZ (Reilinger et al., 2006), (b) the inhomogeneous nature of the material (Şengör et al., 2019b) within the extruding wedge or (c) both of them. Moreover, a zone of higher convergent strain, which is well marked along compressional structures of Muş and Lake Van folds and thrusts in the eastern Anatolia, cuts the EASZ and penetrates into the interior parts of Anatolian Scholle (III′ and III′ in fig 11C′of Şengör et al., 1985). Şengör et al. (1985) also suggest that regions at each side, to the north and south, of this zone of higher convergent strain may may experience different amounts of strain, and the corresponding strike-slip fault segments north and south of the zone may become nonparallel, creating further complexities in their evolution. Not only the rotated geometry of the OF in its western parts but also the compressional component of deformation in this particular section can be explained within the frame of the double high-convergence strain zone model. Therefore, we suggest that the internal deformation of Anatolia is mainly linked with its boundary conditions, the continental collision of Arabia and Eurasia in the east and the Hellenic Subduction in the west, which directly control the style of deformation within its central to eastern parts. Moreover, the "exponential curve" geometries of the 'slip lines' are controlled by the inhomogeneity of the material within Anatolia, mostly by the distribution of the Tethyan accretionary complexes (Şengör et al., 2019b) and the different amount of strain accumulation along the boundaries and/or a high convergent strain zone. The counterclockwise rotation in the strike of southern segments of the CAFZ and MOFZ, creating an obliquity between the slip direction and the fault geometry, may also suggest a reasoning for the extension in these parts (Aktuğ et al., 2013a; Aktuğ et al., 2013b; Yıldırım et al., 2016) as an alternative to the asthenosphere upwelling hypothesis of Yıldırım et al. (2016).

Briefly, we suggest that Anatolia, especially its central and eastern parts, is not a perfect rigid body, but it is sliced by secondary strike-slip faults to several pieces such as the Malatya-Erzincan, Cappadocian (Şengör et al., 2019a), and Central Anatolian slices. This is similar to the model of Higgins et al. (2015), but with a major change in boundary geometries and relative velocities of slices. In our configuration, the CAFZ does not prolong and meet with the NASZ, but it rotates clockwise along its strike to northeast and gains E-W strike and the thrust behaviour (becoming the Divriği Fault) as it is mapped like that in many studies (e.g., Emre et al., 2013; Şengör and Zabcı, 2019). The OF makes the direct boundary between the Central Anatolian and Malatya-Erzincan slices, whereas the MF and the CAFZ are the eastern and western boundaries of the Capaddocian Slice with the Malatya-Erzincan and Central Anatolian slices, respectively. This configuration also well explains the velocity difference between our result on the OF and the very long-term slip-rate of the MF, which drives the slices relatively faster from east to west (i.e. x mm/a for the Malatya-Erzincan Slice, x + 1 mm/a for the Cappadocian Slice, and x + 2.5 mm/a for the Central Anatolian Slice; Figure 14b). The locations of secondary strike-slip faults are strongly controlled by distribution of Tethyan accretionary complexes (Figure 14a and see Şengör et al. (2019b) for detailed information). This also explains the misfit between slip lines of the ideal passive Prandtl cell model and the distribution of these tectonic structures (Figures 14a and 14b). The formation of such secondary and shallow faults is common in plate boundary zones of various origins such as the array of structures between the Garlock and San Andreas faults at the Mojave Desert, southern California (Bohannon and Howell, 1982; Cummings, 1976), secondary faults between the Altay and the Gobi-Altay shear zones (Bayasgalan et al., 1999; Bayasgalan et al., 2005). Thus, it is important to study many aspects of these structures, including their geometries, kinematics, deformation rate, and the inhomogeneity (or homogeneity) of the continental block itself, to have a better understanding on their evolution and seismicity, as it is clearly seen in the case of Anatolia.

7. Conclusion

The integrated analyses of displaced landforms and cosmogenic ^{36}Cl chronology at the Köseler Site provide information about the history of deformation along the OF. We measured two independent risers, NF1/T2 and NF1/NF1', being displaced 15–22 m and 19–24 m, respectively. The surface exposure ages and modelled depth profile ages yield slip-rate estimates, 1.5 +0.4/–0.3 mm/a and 2.8 +0.7/–0.7 mm/a, respectively for the lower-tread reconstruction of the NF1/T2 and 1.4 +0.3/–0.3 mm/a and 2.4 +0.5/–0.4 mm/a, respectively, for the upper-tread reconstruction of the NF1/NF1'. The scatter of surface exposure ages and distribution of ^{36}Cl concentrations in the depth profile together suggest strong inheritance within the alluvial fan and the terrace deposits; thus, we prefer higher rates, which are based on the modelled depth profile ages, for the last 10 ka history of the Ovacık Fault (OF). These geologic slip-rate estimates simply exceed the geodetic rates of the OF or most of the other morphochronology-based velocities along the NE-striking sinistral strike-slip faults

of Anatolia, including the one on the Malatya Fault (MF), the southern member of the Malatya-Ovacık Fault Zone (MOFZ).

The NE-striking sinistral and NW-striking dextral strike-slip faults correspond to the slip lines of a passive Prandtl cell model of Varnes (1962), where the boundary faults move toward each other and the material between the plates moves away from the apex of the wedge. These secondary faults slice Anatolia into several pieces giving formation of the Malatya-Erzincan, Cappadocian, and Central Anatolian slices, where the geometry is strongly controlled by the distribution of weak zones, the Tethyan accretionary complexes. This configuration and relative motion of these slices also well explain the velocity difference between our result on the OF and the very long-term slip-rate of the MF and other structures of internal Anatolia.

Acknowledgements

This study was funded by the TÜBİTAK grant no. 114Y227 and İTÜ BAP project no. MAB-2017-40586. The first author was also supported by Deutscher Akademischer Austauschdienst (DAAD) with the research grant no. 57214227. The stereoscopic aerial photos were supplied by the General Directorate of Mapping. We are thankful to the Ovacık Municipality and people of Ovacık for their great support during our field studies. Sinem Hacıosmanoğlu helped in input of some field and remote sensing data to the Geographical Information System while Alican Aktağ participated in our field studies. We thank Boris A. Natal'in for discussions on tectonics of Anatolia. Critics of Volkan Karabacak and an anonymous reviewer significantly increased the quality of this article. Some figures were made by using the Generic Mapping Tools (Wessel et al., 2013).

References

Acarel D, Cambaz MD, Turhan F, Mutlu AK, Polat R (2019). Seismotectonics of Malatya Fault, Eastern Turkey. Open Geosciences 11 (1): 1098-1111. https://doi.org/10.1515/geo-2019-0085

Akçar N, Ivy-Ochs S, Kubik P, Schlüchter C (2011). Post-depositional impacts on 'Findlinge' (erratic boulders) and their implications for surface-exposure dating. Swiss Journal of Geosciences 104 (3): 445-453.

Akçar N, Tikhomirov D, Özkaymak Ç, Ivy-Ochs S, Alfimov V et al. (2012). ^{36}Cl exposure dating of paleoearthquakes in the Eastern Mediterranean: First results from the western Anatolian Extensional Province, Manisa fault zone, Turkey. Geological Society of America Bulletin, 124 (11-12): 1724-1735.

Akçar N, Yavuz V, Yeşilyurt S, Ivy-Ochs S, Reber R et al. (2017). Synchronous Last Glacial Maximum across the Anatolian peninsula. Geological Society London, Special Publications 433: 251-269. https://doi.org/10.1144/SP433.7

Aktuğ B, Dikmen Ü, Doğru A, Özener H (2013a). Seismicity and strain accumulation around Karliova Triple Junction (Turkey). Journal of Geodynamics 67: 21–29. https://doi.org/10.1016/j.jog.2012.04.008

Aktuğ B, Parmaksız E, Kurt M, Lenk O, Kılıçoğlu A et al. (2013b). Deformation of Central Anatolia: GPS implications. Journal of Geodynamics 67: 78–96. https://doi.org/10.1016/j.jog.2012.05.008

Akyüz HS, Uçarkuş G, Altunel E, Doğan B, Dikbaş A (2012). Paleoseismological investigations on a slow-moving active fault in Central Anatolia, Tecer Fault, Sivas. Annals of Geophysics 55 (5): 847–857. https://doi.org/10.4401/ag-5444

Alfimov V, Ivy-Ochs S (2009). How well do we understand production of ^{36}Cl in limestone and dolomite? Quaternary Geochronology 4(6): 462-474.

Arpat E, Şaroğlu F (1975). Türkiye'de Bazı Önemli Genç Tektonik Olaylar. Türkiye Jeoloji Bülteni 18: 91–101.

Avouac J-P, Tapponnier P (1993). Kinematic model of active deformation in central Asia. Geophysical Research Letters 20: 895–898. https://doi.org/10.1029/93GL00128

Baljinnyam I, Bayasgalan A, Borisov BA, Cisternas A, Dem'yanovich MG et al. (1993). Ruptures of Major Earthquakes and Active Deformation in Mongolia and Its Surroundings, Geological Society of America Memoirs 181: 62+iv p. https://doi.org/10.1130/MEM181-p1

Barka AA, Reilinger R (1997). Active Tectonics of the Eastern Mediterranean Region: deduced from GPS, neotectonic and seismicity data. Annals of Geophysics 40 (3): 587–610. https://doi.org/10.4401/ag-3892

Bayasgalan A, Jackson J, Ritz J-F, Carretier S (1999). Field examples of strike-slip fault terminations in Mongolia and their tectonic significance. Tectonics 18: 394–411. https://doi.org/10.1029/1999TC900007

Bayasgalan A, Jackson J, McKenzie D (2005). Lithosphere rheology and active tectonics in Mongolia: relations between earthquake source parameters, gravity and GPS measurements. Geophysical Journal International 163: 1151–1179. https://doi.org/10.1111/j.1365-246X.2005.02764.x

Bayrakdar C, Çılğın Z, Döker MF, Canpolat E (2015). Evidence of an active glacier in the Munzur Mountains, eastern Turkey. Turkish Journal of Earth Sciences 24: 56–71. https://doi.org/10.3906/yer-1403-7

Blair TC, McPherson JG (1994). Alluvial Fan Processes and Forms. In: Abrahams AD, Parsons AJ (editors) Geomorphology of Desert Environments. Springer Netherlands. pp. 354–402. https://doi.org/10.1007/978-94-015-8254-4_14

Bohannon RG, Howell DG (1982). Kinematic evolution of the junction of the San Andreas, Garlock, and Big Pine faults, California. Geology 10: 358–363. https://doi.org/10.1130/0091-7613(1982)10<358:keotjo>2.0.co;2

Bozkurt E (2001). Neotectonics of Turkey; a synthesis. Geodinamica Acta 14: 3–30.

Chorowicz J, Luxey P, Rudant JP, Lyberis N, Yürür T et al. (1995). Slip-motion estimation along the Ovacik fault near Erzincan (Turkey) using ERS-1 radar image: Evidence of important deformation inside the Turkish plate. Remote Sensing of Environment 52: 66–70. https://doi.org/10.1016/0034-4257(95)00014-R

Chorowicz J, Dhont D, Gündogdu N (1999). Neotectonics in the eastern North Anatolian fault region (Turkey) advocates crustal extension: mapping from SAR ERS imagery and Digital Elevation Model. Journal of Structural Geology 21: 511–532.

Çılğın Z (2020). 3D surface modeling of late Pleistocene glaciers in the Munzur Mountains (Eastern Turkey) and its paleoclimatic implications. Turkish Journal of Earth Sciences 29 (5): 714-732. https://doi.org/10.3906/yer-1905-18

Cowgill E (2007). Impact of riser reconstructions on estimation of secular variation in rates of strike-slip faulting: Revisiting the Cherchen River site along the Altyn Tagh Fault, NW China. Earth and Planetary Science Letters 254 (3-4): 239–255. https://doi.org/10.1016/j.epsl.2006.09.015

Cummings D (1976). Theory of plasticity applied to faulting, Mojave Desert, southern California. Geological Society of America Bulletin 87: 720–724.

Desilets D, Zreda M, Almasi PF, Elmore D (2006). Determination of cosmogenic ^{36}Cl in rocks by isotope dilution: innovations, validation and error propagation. Chemical Geology 233 (3–4): 185-195. https://doi.org/10.1016/j.chemgeo.2006.03.001

Dunai TJ (2010). Cosmogenic Nuclides: Principles, Concepts and Applications in the Earth Surface Sciences. Cambridge University Press, Cambridge. https://doi.org/10.1017/CBO9780511804519

Dunne J, Elmore D, Muzikar P (1999). Scaling factors for the rates of production of cosmogenic nuclides for geometric shielding and attenuation at depth on sloped surfaces. Geomorphology 27 (1–2): 3-11.

Ekström G, Nettles M, Dziewoński AM (2012). The global CMT project 2004–2010: Centroid-moment tensors for 13,017 earthquakes. Physics of the Earth and Planetary Interiors 200–201: 1–9. https://doi.org/10.1016/j.pepi.2012.04.002

Elmore D, Ma X, Miller T, Mueller K, Perry M et al. (1997). Status and plans for the PRIME Lab AMS facility. Nuclear Instruments and Methods in Physics Research Section B: Beam Interactions with Materials and Atoms, 123(1): 69-72.

Emre Ö, Duman TY, Özalp S, Elmacı H, Olgun Ş et al. (2013). Açıklamalı Türkiye Diri Fay Haritası Ölçek 1:1250000 (Active Fault Map of Turkey with an Explanatory Text 1:1250000 scale). Maden Tetkik ve Arama Genel Müdürlüğü, Ankara.

England P, Houseman G, Nocquet J-M (2016). Constraints from GPS measurements on the dynamics of deformation in Anatolia and the Aegean. Journal of Geophysical Research: Solid Earth 121: 8888–8916. https://doi.org/10.1002/2016JB013382

Evans JM, Stone JOH, Fifield LK, Cresswell RG (1997). Cosmogenic Chlorine-36 production in K-feldspar. Nuclear Instruments and Methods in Physics Research Section B: Beam Interactions with Materials and Atoms 123 (1): 334-340.

Fabryka-Martin JT (1988). Production of Radionuclides in the Earth and Their Hydrogeologic Significance with Emphasis on Chlorine-36 and Iodine-129. PhD, Arizona University.

Faccenna C. Becker TW, Jolivet L, Keskin M (2013). Mantle convection in the Middle East: Reconciling Afar upwelling, Arabia indentation and Aegean trench rollback. Earth and Planetary Science Letters 375: 254–269. https://doi.org/http://dx.doi.org/10.1016/j.epsl.2013.05.043

Göğüş OH, Pysklywec RN, Şengör AMC, Gün E (2017). Drip tectonics and the enigmatic uplift of the Central Anatolian Plateau. Nature Communications 8: 1538. https://doi.org/10.1038/s41467-017-01611-3

Gold RD, Cowgill E, Arrowsmith JR, Gosse J, Chen X et al. (2009). Riser diachroneity, lateral erosion, and uncertainty in rates of strike-slip faulting: A case study from Tuzidun along the Altyn Tagh Fault, NW China. Journal of Geophysical Research: Solid Earth 114: B04401. https://doi.org/10.1029/2008jb005913

Gold RD, Cowgill E, Arrowsmith JR, Chen X, Sharp WD et al. (2011). Faulted terrace risers place new constraints on the late Quaternary slip-rate for the central Altyn Tagh fault, northwest Tibet. Geological Society of America Bulletin 123: 958–978. https://doi.org/10.1130/b30207.1

Gürsoy H, Piper JDA, Tatar O, Temiz H (1997). A palaeomagnetic study of the Sivas Basin, central Turkey: crustal deformation during lateral extrusion of the Anatolian Block. Tectonophysics 271: 89–105. https://doi.org/10.1016/s0040-1951(96)00242-9

Haddon EK, Amos CB, Zielke O, Jayko AS, Bürgmann R (2016). Surface slip during large Owens Valley earthquakes. Geochemistry, Geophysics, Geosystems 17 (6): 2239–2269. https://doi.org/10.1002/2015GC006033

Hancock GS, Anderson RS, Chadwick OA, Finkel, RC (1999). Dating fluvial terraces with ^{10}Be and ^{26}Al profiles: application to the Wind River, Wyoming. Geomorphology 27 (1–2): 41-60.

Higgins M, Schoenbohm LM, Brocard G, Kaymakçı N, Gosse JC et al. (2015). New kinematic and geochronologic evidence for the Quaternary evolution of the Central Anatolian fault zone (CAFZ). Tectonics 34: 2118–2141. https://doi.org/10.1002/2015TC003864

Ivy-Ochs S, Dühnforth M, Densmore AL, Alfimov V (2013). Dating fan deposits with cosmogenic nuclides. In: M.S.-B.e. al. (editors), Dating torrential processes on fans and cones. Advances in Global Change Research. Springer, Dordrecht, pp. 243-263.

Ivy-Ochs S, Kober F (2008). Surface exposure dating with cosmogenic nuclides. Eiszeitalter und Gegenwart Quaternary Science Journal 57 (1-2): 179-209.

Ivy-Ochs S, Schäfer J, Kubik PW, Synal H-A, Schlüchter C (2004). Timing of deglaciation on the northern Alpine foreland (Switzerland). Eclogae Geologicae Helvetiae 97 (1): 47-55.

Kandilli Rasathanesi ve Deprem Araştırma Enstitüsü (2020). B.U. KOERI-RETMC Earthquake Catalog [WWW Document]. URL http://www.koeri.boun.edu.tr/sismo/2/earthquake-catalog/ (accessed 1.8.20).

Kaymakçı N, İnceöz M, Ertepınar P (2006). 3-D Architecture and Neogene Evolution of the Malatya Basin: Inferences for the Kinematics for the Malatya and Ovacık Fault Zone. Turkish Journal of Earth Sciences 15: 123–154.

Koçyiğit A, Beyhan A (1998). A new intracontinental transcurrent structure: the Central Anatolian Fault Zone, Turkey. Tectonophysics 284: 317–336. https://doi.org/10.1016/s0040-1951(97)00176-5

Kurushin RA, Bayasgalan A, Ölziybat M, Enhtuvshin B, Molnar P et al. (1997). The Surface Rupture of the 1957 Gobi-Altay, Mongolia, Earthquake, Geological Society of America Special Paper. Boulder, Colorado. https://doi.org/10.1130/SPE320

Lal D (1991). Cosmic ray labeling of erosion surfaces: in situ nuclide production rates and erosion models. Earth and Planetary Science Letters, 104 (2): 424-439.

Le Dortz K, Meyer B, Sébrier M, Braucher R, Bourlès D et al. (2012). Interpreting scattered in-situ produced cosmogenic nuclide depth-profile data. Quaternary Geochronology 11: 98–115. https://doi.org/10.1016/j.quageo.2012.02.020

Le Pichon X (1968). Sea-floor spreading and continental drift. Journal of Geophysical Research 73: 3661–3697. https://doi.org/10.1029/JB073i012p03661

Le Pichon X, Kreemer C (2010). The Miocene-to-Present Kinematic Evolution of the Eastern Mediterranean and Middle East and Its Implications for Dynamics. Annual Review of Earth and Planeteary Sciences 38: 323–351. https://doi.org/doi:10.1146/annurev-earth-040809-152419

Liu B, Phillips FM, Fabryka-Martin JT, Fowler MM, Stone WD (1994). Cosmogenic ^{36}Cl accumulation in unstable landforms: 1. Effects of the thermal neutron distribution. Water Resources Research, 30(11): 3115-3125.

McKenzie DP (1970). Plate Tectonics of the Mediterranean Region. Nature 226: 239–243.

McKenzie DP (1972). Active Tectonic of the Mediterranean Region. Geophysical Journal of Royal Astronomical Society 30:109–185.

McKenzie DP, Parker RL (1967). The North Pacific: an Example of Tectonics on a Sphere. Nature 216: 1276–1280.

Meade BJ, Hager BH (2005). Block models of crustal motion in southern California constrained by GPS measurements. Journal of Geophysical Research 110: B03403. https://doi.org/10.1029/2004jb003209

Mériaux AS, Ryerson FJ, Tapponnier P, Van der Woerd J, Finkel RC et al. (2004). Rapid slip along the central Altyn Tagh Fault: Morphochronologic evidence from Cherchen He and Sulamu Tagh. Journal of Geophysical Research Solid Earth 109: B06401 https://doi.org/10.1029/2003JB002558

Mériaux AS, Tapponnier P, Ryerson FJ, Xiwei X, King G et al. (2005). The Aksay segment of the northern Altyn Tagh fault: Tectonic geomorphology, landscape evolution, and Holocene slip rate. Journal Geophysical Research Solid Earth 110: B04404. https://doi.org/10.1029/2004JB003210

Mériaux AS, Van der Woerd J, Tapponnier P, Ryerson FJ, Finkel RC et al. (2012). The Pingding segment of the Altyn Tagh Fault (91°E): Holocene slip-rate determination from cosmogenic radionuclide dating of offset fluvial terraces. Journal of Geophysical Research Solid Earth 117: B09406. https://doi.org/10.1029/2012JB009289

Molnar P (1988). Continental tectonics in the aftermath of plate tectonics. Nature 335: 131–137. https://doi.org/10.1038/335131a0

Molnar P, Tapponnier P (1975). Cenozoic Tectonics of Asia: Effects of a Continental Collision. Science 189: 419-426. https://doi.org/10.1126/science.189.4201.419

Morgan WJ (1968). Rises, trenches, great faults, and crustal blocks. Journal of Geophysical Research 73: 1959–1982. https://doi.org/10.1029/JB073i006p01959

Okal EA (1977). The July 9 and 23, 1905, Mongolian earthquakes: A surface wave investigation. Earth and Planeteary Science Letters 34: 326–331. https://doi.org/10.1016/0012-821X(77)90018-8

Özbey V, Şengör AMC, Özeren MS (2022). Tectonics in a very slowly deforming region in an orogenic belt. Tectonophysics 827: 229272. https://doi.org/10.1016/j.tecto.2022.229272

Özener H, Arpat E, Ergintav S, Doğru A, Çakmak R et al. (2010). Kinematics of the eastern part of the North Anatolian Fault Zone. Journal of Geodynamics 49: 141–150. https://doi.org/10.1016/j.jog.2010.01.003

Özeren, MS, Holt WE (2010). The dynamics of the eastern Mediterranean and eastern Turkey. Geophysical Journal International 183: 1165–1184. https://doi.org/10.1111/j.1365-246X.2010.04819.x

Paul A, Karabulut H, Mutlu AK, Salaün G. (2014). A comprehensive and densely sampled map of shear-wave azimuthal anisotropy in the Aegean–Anatolia region. Earth and Planetary Science Letters 389: 14–22. https://doi.org /10.1016/j.epsl.2013.12.019

Pérouse E, Sébrier M, Braucher R, Chamot-Rooke N, Bourlès D et al. (2017). Transition from collision to subduction in Western Greece: the Katouna–Stamna active fault system and regional kinematics. International Journal of Earth Sciences 106: 967–989. https://doi.org/10.1007/s00531-016-1345-9

Phillips FM, Stone WD, Fabryka-Martin JT (2001). An improved approach to calculating low-energy cosmic-ray neutron fluxes near the land/atmosphere interface. Chemical Geology 175 (3–4): 689-701.

Reilinger R, McClusky S, Vernant P, Lawrence S, Ergintav S et al. (2006). GPS constraints on continental deformation in the Africa-Arabia-Eurasia continental collision zone and implications for the dynamics of plate interactions. Journal of Geophysical Research Solid Earth 111: B05411. https://doi.org/10.1029/2005JB004051

Sançar T, Akyüz HS, Schreurs G, Zabcı C (2018). Mechanics of Plio-Quaternary faulting around the Karliova triple junction: implications for the deformation of eastern part of the Anatolian Scholle. Geodinamica Acta 30: 287–305. https://doi.org/10.1080/09853111.2018.1533736

Sançar T, Zabcı C, Karabacak V, Yazıcı M, Akyüz HS (2019). Geometry and Paleoseismology of the Malatya Fault (Malatya-Ovacık Fault Zone), Eastern Turkey: Implications for intraplate deformation of the Anatolian ScholleJournal of Seismology 23: 319–340. https://doi.org/10.1007/s10950-018-9808-z

Sançar T, Zabcı C, Akçar N, Karabacak V, Yeşilyurt S et al. (2020). Geodynamic importance of the strike-slip faults at the eastern part of the Anatolian Scholle: Inferences from the uplift and slip-rate of the Malatya Fault (Malatya-Ovacık Fault Zone, eastern Turkey). Journal of Asian Earth Sciences 188: 104091. https://doi.org/10.1016/j.jseaes.2019.104091

Sarıkaya MA, Yıldırım C, Çiner A (2015). No surface breaking on the Ecemiş Fault, central Turkey, since Late Pleistocene (~64.5 ka); new geomorphic and geochronologic data from cosmogenic dating of offset alluvial fans. Tectonophysics 64: 33–46. https://doi.org/10.1016/j.tecto.2015.02.022

Schildgen TF, Cosentino D, Caruso A, Buchwaldt R, Yıldırım C et al. (2012). Surface expression of eastern Mediterranean slab dynamics: Neogene topographic and structural evolution of the southwest margin of the Central Anatolian Plateau, Turkey. Tectonics 31: TC2005. https://doi.org/10.1029/2011tc003021

Schildgen TF, Yıldırım C, Cosentino D, Strecker MR (2014). Linking slab break-off, Hellenic trench retreat, and uplift of the Central and Eastern Anatolian plateaus. Earth-Science Reviews 128: 147–168. https://doi.org/10.1016/j.earscirev.2013.11.006

Schlupp A, Cisternas A (2007). Source history of the 1905 great Mongolian earthquakes (Tsetserleg, Bolnay). Geophysical Journal International 169: 1115–1131. https://doi.org/10.1111/j.1365-246X.2007.03323.x

Şengör AMC (1979). The North Anatolian transform fault; its age, offset and tectonic significance. Journal of Geological Society 136 (3): 269–282. https://doi.org/10.1144/gsjgs.136.3.0269

Şengör AMC (1980). Türkiye'nin neotektoniğinin esasları (Principles of the Neotectonism of Turkey). Türkiye Jeoloji Kurumu Konferans Serisi, Ankara.

Şengör AMC, Natal'in BA, Burtman VS (1993). Evolution of the Altaid tectonic collage and Palaeozoic crustal growth in Eurasia. Nature 364: 299–307. http://dx.doi.org/10.1038/364299a0

Şengör AMC, Natalin BA (1996). Paleotectonics of Asia: Fragments of a Synthesis. In: Yin A, Harrison M (editors), The Tectonic Evolution of Asia. Cambridge University Press, Cambridge, pp. 486–640.

Şengör AMC, Görür N, Şaroğlu F (1985). Strike-slip faulting and related basin formation in zones of tectonic escape: Turkey as a case study. In: Biddle KT, Christie-Blick N (editors), Strike-Slip Deformation, Basin Formation, and Sedimentation, Society of Economic Paleontologists and Mineralogists Special Publication, Oklahoma, vol. 37 pp. 227–264. https://doi.org/10.2110/pec.85.37.0211

Şengör AMC, Natal'in BA, Sunal G, van der Voo R (2018). The Tectonics of the Altaids: Crustal Growth During the Construction of the Continental Lithosphere of Central Asia Between ~750 and ~130 Ma Ago. Annual Review of Earth and Planetary Sciences 46 (1): 439–494. https://doi.org/10.1146/annurev-earth-060313-054826

Şengör AMC, Zabcı C, Natal'in BA (2019a). Continental Transform Faults: Congruence and Incongruence with Normal Plate Kinematics. In: Duarte JC (editor), Transform Plate Boundaries and Fracture Zones. Elsevier, pp. 169–247. https://doi.org/https://doi.org/10.1016/B978-0-12-812064-4.00009-8

Şengör AMC, Lom N, Sunal G, Zabcı C, Sançar T. (2019b). The phanerozoic palaeotectonics of Turkey. Part I: an inventory. Mediterranean Geoscience Reviews 1: 91–161. https://doi.org/10.1007/s42990-019-00007-3.

Şengör AMC, Yazıcı M (2020) The aetiology of the neotectonic evolution of Turkey. Mediterranean Geoscicence Reviews 2:327–339. https://doi.org/10.1007/s42990-020-00039-0

Sieh KE, Jahns RH (1984). Holocene activity of the San Andreas fault at Wallace Creek, California. Geological Society of America Bulletin 95: 883–896. https://doi.org/10.1130/0016-7606(1984)95<883:haotsa>2.0.co;2

Stange KM, van Balen R, Carcaillet J, Vandenberghe J (2013). Terrace staircase development in the Southern Pyrenees Foreland: Inferences from ^{10}Be terrace exposure ages at the Segre River. Global and Planetary Change 101: 97–112. https://doi.org/10.1016/j.gloplacha.2012.12.007

Stein S, Sella GF (2002). Plate Boundary Zones: Concepts and Approaches. In Stein S, Freymueller (editors) Plate Boundary Zones, Geodynamics Series. https://doi.org/doi:10.1029/GD030p0001

Stone JO (2000). Air pressure and cosmogenic isotope production. Journal of Geophysical Research: Solid Earth 105 (B10): 23753-23759. https://doi.org/10.1029/2000JB900181

Stone JO, Allan GL, Fifield LK, Cresswell RG (1996). Cosmogenic Chlorine-36 from calcium spallation. Geochimica et Cosmochimica Acta 60 (4): 679-692. https://doi.org/10.1016/0016-7037(95)00429-7

Stone JOH, Evans JM, Fifield LK, Allan GL, Cresswell RG (1998). Cosmogenic Chlorine-36 Production in Calcite by Muons. Geochimica et Cosmochimica Acta 62 (3): 433-454. https://doi.org/10.1016/S0016-7037(97)00369-4

Synal HA, Bonani G, Döbeli M, Ender RM, Gartenmann P, Kubik PW, Schnabel C, Suter M (1997). Status report of the PSI/ETH AMS facility. Nuclear Instruments and Methods in Physics Research Section B: Beam Interactions with Materials and Atoms 123 (1): 62-68. https://doi.org/10.1016/S0168-583X(96)00608-8

Tapponnier P, Peltzer G, Armijo R (1986). On the mechanics of the collision between India and Asia. Geological Society London, Special Publications 19: 113–157. https://doi.org/10.1144/GSL.SP.1986.019.01.07

Tarhan N (2008). 1:100.000 ölçekli Türkiye Jeoloji Haritaları, No: 88 Erzincan - J42 Paftası. Maden Tetkik ve Arama Genel Müdürlüğü, Ankara.

Tatar O, Poyraz F, Gürsoy H, Çakır Z, Ergintav S et al. (2012) Crustal deformation and kinematics of the Eastern Part of the North Anatolian Fault Zone (Turkey) from GPS measurements. Tectonophysics 518–521: 55–62. https://doi.org/10.1016/j.tecto.2011.11.010

Tikhomirov D, Akçar N, Ivy-Ochs S, Alfimov V, Schlüchter C (2014). Calculation of shielding factors for production of cosmogenic nuclides in fault scarps. Quaternary Geochronology 19: 181-193. https://doi.org/10.1016/j.quageo.2013.08.004

van der Woerd J, Ryerson FJ, Tapponnier P, Gaudemer Y, Finkel R et al. (1998). Holocene left-slip-rate determined by cosmogenic surface dating on the Xidatan segment of the Kunlun fault (Qinghai, China). Geology 26: 695–698. https://doi.org/10.1130/0091-7613(1998)026<0695:hlsrdb>2.3.co;2

van der Woerd J, Ryerson FJ, Tapponnier P, Mériaux AS, Gaudemer Y et al. (2000). Uniform Slip-Rate along the Kunlun Fault: Implications for seismic behaviour and large-scale tectonics. Geophysical Research Letters 27: 2353–2356. https://doi.org/10.1029/1999GL011292

van der Woerd J, Tapponnier P, Ryerson FJ, Mériaux AS, Meyer B (2002). Uniform postglacial slip-rate along the central 600 km of the Kunlun Fault (Tibet), from Al-26, Be-10, and C-14 dating of riser offsets, and climatic origin of the regional morphology. Geophysical Journal International 148: 356–388. https://doi.org/10.1046/j.1365-246x.2002.01556.x

Varnes DJ (1962). Analysis of plastic deformation according to Von Mises' theory, with application to the South Silverton area, San Juan County, Colorado, USGS Professional Paper, v.378-B. Colorado.

Viveen W, Braucher R, Bourlès D, Schoorl JM, Veldkamp A et al. (2012). A 0.65Ma chronology and incision rate assessment of the NW Iberian Miño River terraces based on ^{10}Be and luminescence dating. Global and Planeteary Change 94–95: 82–100. https://doi.org/10.1016/j.gloplacha.2012.07.001

Weiqi Z, Decheng J, Peizhen Z, Molnar P, Burchfield BC et al. (1987). Displacement along the Haiyuan fault associated with the great 1920 Haiyuan, China, earthquake. Bulletin of the Seismological Society of America 77 (1): 117–131. https://doi.org/10.1785/BSSA0770010117

Wallace RE (1990). General Features. In: Wallace RE (editor), The San Andreas Fault System, California. U.S. Geological Survey, Denver, pp. 8–12.

Wessel P, Smith WHF, Scharroo R, Luis J, Wobbe F (2013). Generic Mapping Tools: Improved Version Released. Eos, Transactions American Geophysical Union 94: 409–410. https://doi.org/10.1002/2013EO450001

Westaway R, Arger J (2001). Kinematics of the Malatya–Ovacık Fault Zone. Geodinamica Acta 14: 103–131. https://doi.org/10.1016/S0985-3111(00)01058-5

Westaway R, Demir T, Seyrek A (2008). Geometry of the Turkey-Arabia and Africa-Arabia plate boundaries in the latest Miocene to Mid-Pliocene: the role of the Malatya-Ovacık Fault Zone in eastern Turkey. Earth 3: 27–35. https://doi.org/10.5194/ee-3-27-2008

Wilson JT (1965). A New Class of Faults and their Bearing on Continental Drift. Nature 207: 343–347.

Yazıcı M, Zabcı C, Sançar T, Natal'in BA (2018). The role of intraplate strike-slip faults in shaping the surrounding morphology: The Ovacık Fault (eastern Turkey) as a case study. Geomorphology 321: 129–145. https://doi.org/10.1016/J.GEOMORPH.2018.08.022

Yeşilyurt S, Akçar N, Doğan U, Yavuz V, Ivy-Ochs S et al. (2015). Extensive ice fields in eastern Turkey during the Last Glacial Maximum, in: INQUA XIX. Nagoya, Japan, p. T00993.

Yıldırım C (2014). Relative tectonic activity assessment of the Tuz Gölü Fault Zone; Central Anatolia, Turkey. Tectonophysics 630: 183–192. https://doi.org/10.1016/j.tecto.2014.05.023

Yıldırım C, Sarıkaya MA, Çiner A (2016). Late Pleistocene intraplate extension of the Central Anatolian Plateau, Turkey: Inferences from cosmogenic exposure dating of alluvial fan, landslide, and moraine surfaces along the Ecemiş Fault Zone. Tectonics 35: 1446–1464. https://doi.org/10.1002/2015TC004038

Zechar JD, Frankel KL (2009). Incorporating and reporting uncertainties in fault slip rates. Journal of Geophysical Research Solid Earth 114: B12407. https://doi.org/10.1029/2009JB006325

Zielke O, Arrowsmith JR (2012). LaDiCaoz and LiDARimager—MATLAB GUIs for LiDAR data handling and lateral displacement measurement. Geosphere 8 (1): 206–221.